

Stellar dynamics in the central arcsecond of our galaxy¹

R. Schödel, T. Ott, R. Genzel¹

Max-Planck-Institut für extraterrestrische Physik, Giessenbachstraße, Garching, Germany

and

A. Eckart, N. Mouawad

I.Physikalisches Institut, Universität zu Köln, Zùlpicher Straße , Köln, Germany

and

T. Alexander

Faculty of Physics, Weizmann Institute of Science, Rehovot, Israel

ABSTRACT

With 10 years of high-resolution imaging data now available on the stellar cluster in the Galactic Center, we present proper motions for >40 stars at projected distances $\leq 1.2''$ from Sagittarius A* (Sgr A*). We find evidence on a $\geq 2\sigma$ level for radial anisotropy of the cluster of stars within $1''$ of Sgr A*. For a brightness limit of $K \sim 15.5$ we find no evidence for a stationary source at the position of Sgr A* or for a source at this position that would be variable on a time scale of at least several hours to days. On time scales of seconds to tens of minutes, we find no variability at the Sgr A* position on brightness levels $K \leq 13.5$. We confirm/find accelerated motion for 6 stars, with 4 stars having passed the pericenter of their orbits during the observed time span. We calculated/constrained the orbital parameters of these stars. All orbits have moderate to high eccentricities. We discuss the possible bias in detecting preferentially orbits with high eccentricities and find that measured values of $e > 0.9$ might be detected by about a factor of $1.5 - 2$ more frequently. We find that the center of acceleration for all the orbits coincides with the radio position of Sgr A*. From the orbit of the star S2, the currently most tightly constrained one, we determine the mass of Sgr A* to be $3.3 \pm 0.7 \times 10^6 M_\odot$ and its position to 2.0 ± 2.4 mas East and 2.7 ± 4.5 mas South of the nominal radio position. The mass estimate

¹Also: Department of Physics, University of California, Berkeley, CA 94720

for the central dark mass from the orbit of S2 is fully consistent with the mass estimate of $3.4 \pm 0.5 \times 10^6 M_{\odot}$ obtained from stellar proper motions within $1.2''$ of Sgr A* using a Leonard-Merritt mass estimator. We find that radio astronomical observations of the proper motion of Sgr A* in combination with its intrinsic source size place at the moment the tightest constraints on the mass density of Sgr A*, which must exceed $\rho_{\text{Sgr A}^*} > 3 \times 10^{19} M_{\odot} \text{pc}^{-3}$.

Subject headings:

1. Introduction

The discovery of quasars and active galactic nuclei gave rise to the idea that massive black holes (MBH) of several million to billion solar masses exist at the centers of active galaxies. Over the last decades, evidence has been accumulated through the observation of stellar and gas dynamics in the centers of nearby galaxies, that most quiet galaxies harbour a MBH at their centers as well, with more than 30 candidates listed in the latest census (Kormendy 2001)³. With the number of putative MBH growing constantly through increasing observational evidence, it has meanwhile become a standard paradigm of modern astronomy that MBHs exist at the centers of the vast majority of galaxies.

A special case is the center of our home galaxy. Located at a distance of only 8 kpc from the solar system (Reid 1993), it allows detailed astrometric observations of stars at distances $\ll 1\text{pc}$ from the central black hole candidate, the radio source Sgr A*. Near-Infrared (NIR) high-resolution imaging and spectroscopic observations with speckle and adaptive optics techniques were carried out during the last decade at 4m to 10m-class telescopes. They allowed to measure the projected and radial motions of ~ 100 stars within the central 0.1 pc as well as the accelerations of a few individual stars as close as a few light days from Sgr A*. The results of these observations made a compelling case that the concentration of dark mass seen at the center of the Milky Way is indeed in the form of a supermassive black hole (Genzel et al. 1996; Eckart & Genzel 1997; Ghez et al. 1998, 2000; Eckart et al. 2002; Schödel et al. 2002).

A series of observations that covered the pericenter passage of the star S2 around Sgr A*, allowed Schödel et al. (2002) to determine a unique keplerian orbit (up to the sign of the

¹Based on observations at the Very Large Telescope (VLT) of the European Southern Observatory (ESO) on Paranal in Chile

³an up-to-date list is maintained at <http://chandra.as.utexas.edu/~kormendy/bhsearch.html>

inclination) for this object and to measure the enclosed dark mass down to a distance of a mere 17 light hours from Sgr A*. With these observations, they could exclude with high confidence a neutrino ball scenario (Munyanza & Viollier 2002) as an alternative explanation for the dark mass concentration as well as a cluster of dark astrophysical objects (Maoz 1998), such as neutron stars, leaving a central supermassive black hole as the only plausible explanation. Recently, Ghez et al. (2003) confirmed the orbit of S2, presenting also the first line-of-sight velocity measurements for this star.

With the nature of the dark central object now being known to a high degree of confidence, we want to understand the interactions of the black hole with its environment and its impact on the population of surrounding stars and their dynamics. In this paper we provide a high-quality data base of proper motions and accelerations of the stars in the immediate environment of Sgr A*, on scales of $\sim 1''$, or 0.04 pc (for a Galactic Center distance of 8 kpc (Reid 1993), which will be assumed throughout this paper). With these data we analyze the dynamics of this region which is dominated by the stellar cusp around Sgr A* that was found in deep adaptive optics (AO) observations by Genzel et al. (2003).

2. Observations and data reduction

We compiled observations from three different data sets for the present work. Near-infrared (NIR) speckle imaging observations with the MPE-built NIR speckle imaging camera SHARP (Hofmann et al. 1995) were carried out at the ESO 3.5m NTT in La Silla, Chile, from 1992 to 2002. For the year 2000 we included the publicly available Gemini North Observatory Galactic Center Demonstration Science Data Set. For the 2002 epoch we used the commissioning and science verification AO observations of the GC with the new NAOS/CONICA adaptive optics system/NIR camera (constructed by MPIA/MPE, Meudon/Grenoble Observatories, ONERA, ESO) on the ESO VLT unit telescope 4 (Yepun) on El Paranal, Chile (Rousset et al. 1998; Lenzen et al. 1998). The latter data are publicly available in the ESO archive and some of the first results have been published by Schödel et al. (2002) and Genzel et al. (2003). The individual data sets and their processing are described in more detail in the following sections. Standard data reduction procedures, i.e. sky subtraction, dead/bad pixel masking, and flat-fielding, were applied to all the imaging data.

2.1. The SHARP/NTT imaging data

Imaging data with the MPE speckle camera SHARP were obtained once or twice every year since 1992, with the instrument used as a guest instrument at the ESO NTT. An integration time of 0.5 s was used for the individual imaging frames. This was found to be the best choice for achieving an optimal signal-to-noise ratio while at the same time still conserving the diffraction limited information. From the several tens of thousands of individual speckle frames obtained in each observing epoch, we pre-selected ~ 1000 high-quality frames automatically. Selection criterion was the number of bright speckles of the dominant star in a frame: Beside the brightest speckle, there should not be more than one additional speckle with more than 10% of the flux of the brightest speckle. From the pre-selected frames we picked by eye several hundred speckle frames with the highest quality. Selection criterion was that the first diffraction ring around the dominant speckle of the brightest stars must be clearly visible in these individual 0.5 s exposures. For every observing epoch, the final selection of highest quality images was divided into ~ 4 subsets of about one hundred frames each. After combining the frames of such a subset with a simple shift-and-add algorithm, the Strehl ratio was found to be of the order 30% in the final images.

We applied Iterative Blind Deconvolution (IBD) (Jeffries & Christou 1993) on the sets of high-quality speckle frames. IBD iteratively reconstructs the object and the point spread function of an image from initial estimates. It makes use of some general constraints on the imaging properties, e.g. the positivity of object and PSF and that the convolution of the object with the PSF must yield the original image again (in case of zero noise). In the case of speckle imaging, we have multiple images of the same object. IBD can take use of that information effectively. It reconstructs the observed object and at the same time the individual PSFs for each speckle frame. Convergence of the IBD algorithm is guided via an error metric that describes the deviation of the PSFs and object estimates from their constraints.

We used the publicly available IDAC program code ⁴. The shift-and-add images of the sets of speckle frames were used for the initial estimates. Because of the high demand of computing time for this algorithm, we applied it only to a $\sim 6 \times 6''$ area around Sgr A* that included the IRS 16 complex of bright ($K \sim 10$) sources. After convergence of the IBD algorithm, the resulting 3 to 4 object images for every observing epoch were oversampled to a third of the original pixel scale, smoothed and coadded. Any remaining PSF residuals were then cleaned with a Lucy-Richardson deconvolution. We produced final maps by restoring

⁴developed at Steward Observatory by Matt Chesalka and Keith Hege (based on the earlier Fortran Blind Deconvolution code - IDA - developed by Stuart Jeffries and Julian Christou)

the result of the deconvolution with a Gaussian beam of 100 mas FWHM.

We also produced maps in a similar way by using the Lucy-Richardson (LR) algorithm instead of the IDAC code and the shift-and-add images instead of the individual speckle frames. The maps compare very well with the maps produced with the aid of the IDAC code. However, we found that the IDAC procedure provided maps of practically constant quality for all epochs, while the quality is slightly more variable in the case of the LR algorithm. A possible cause for this may be that one needs to use a PSF estimate for a LR deconvolution. We used the bright, isolated source IRS 7 as PSF reference. It is ~ 5 magnitudes brighter than any other star in its immediate surroundings and is thus very well suited as a PSF reference. However, in some cases the PSF reference was not contained in the FOV, in other cases the anisoplanatic angle might have been small. Therefore the results of the LR deconvolved maps are of slightly more variable quality than the IBD maps and we decided to use the latter in our further analysis because they guarantee an equal treatment and quality of all the maps.

One of the strengths of the IBD/IDAC routine is that it can use *multiple* images of the *same* object at the same time, which poses tight constraints on the object distribution. Thus, the final object can be reconstructed reliably. A further advantage of IBD is that one does not need an accurate estimate of the PSF for a reliable deconvolution. On the negative side, one has to mention the considerable amount of computing time needed for the IBD algorithm.

In the described way, we obtained high-resolution maps for all epochs, except for 1993 and 2002, where the quality of the imaging data did not allow to select a sufficiently large sample of high-quality speckle frames. The 1992 speckle frames are characterised by a fairly strong readout “waffle” pattern. While the resulting high-resolution map for 1992 compares favourably with the other epochs, the stellar positions may be subject to larger errors for this epoch.

Our method here is optimized for producing the deepest ($K(3-5\sigma)\approx 16$) diffraction limited SHARP/NTT maps of comparable quality for all observing epochs. This is in contrast to our earlier work, such as Eckart & Genzel (1997). There, deep high-resolution maps were produced only for a few selected epochs. The approach of Ott et al. (2003) is also distinct from the approach presented here: They produced and analyzed in a largely automated, efficient way several tens of shift-and-add images for every SHARP observing period. While their maps allow to effectively determine proper motions for ~ 1000 stars in a $\sim 10''$ radius region around Sgr A*, they are generally ~ 0.5 to 1 magnitude shallower and of more variable quality than the maps used in this work, which serve the purpose to examine the proper motions in the very central, most crowded part of the cluster, and for the weakest

sources possible. The Ott et al. (2003) approach and our approach presented here can be seen as mutually complementary.

In order to verify the SHARP high-resolution maps, we compared them among each other to check whether the identified sources and proper motions were consistent between the epochs (see section 3). An additional check was made by a comparison between the IBD and the LR deconvolved maps. For the epochs around 2000, we also compared the SHARP maps with the maps obtained from the Gemini and NACO data sets (see below). In Figure 1 we show the the Gemini 2000, the SHARP 2001 (IBD and LR), and NACO 2002 maps, all of them restored to a FWHM of ~ 100 mas.

2.2. The Gemini imaging data

In addition to our SHARP map for the epoch 2000, we selected one K'-band image from the publicly available Gemini North Observatory Galactic Center Demonstration Science Data Set. This data set provides observations of the Galactic Center stellar cluster with the Gemini North telescope, the Quirc near infrared camera and the Hokupa'a AO system. We selected an image of 750 s total integration time, observed in July 2000. Since the Hokupa'a AO system was designed for a 4m-class telescope, it could only partially provide the correction needed for the 8m-class Gemini telescope. Moreover, the visible guiding star used for the observations is located at $\sim 30''$ from Sgr A*, so the Strehl ratio of the image is rather low. However, the central sources around Sgr A* are clearly resolved at an estimated resolution of 100 mas.

We created a PSF from the median of ~ 15 bright, unsaturated stars in the image. Because the wings of the PSF were very strong, but contaminated by weak sources, we fitted the wings of the PSF with a Moffat function. Subsequently, we created a model PSF by combining the model for the wings with the PSF Kernel obtained by the median of the stellar images. This PSF model was used for a LR deconvolution of the K'-band image, which was reconvolved to a final map with a Gaussian beam of ~ 100 mas FWHM. We did not use the IDAC algorithm because it works less well in case there is only one image of a given object.

2.3. The NAOS/CONICA imaging data

The GC stellar cluster was observed several times during the commissioning and science verification of the NAOS/CONICA (“NACO”) AO system and near infrared camera at the ESO VLT unit telescope 4. With its unique infrared wavefront sensor, the loop of the AO

was closed on the $K \sim 6.5$ mag supergiant IRS 7, which is located $\sim 5.5''$ north of Sgr A*. We chose K' -band observations from May 2002 (30 frames with 30 s integration time) and from August 2002 (20 frames with 60 s integration time). The individual frames were coadded to images with a total of 900 s (May) and 1200 s (August) integration time. In the August observation run, a Strehl ratio of $> 50\%$ was achieved. A description of the NACO imaging data can also be found in Genzel et al. (2003) and Ott et al. (2003a).

We used ~ 15 stars in each image to extract a median PSF, which was used for a Lucy-Richardson deconvolution. Final maps were obtained after restoration with a Gaussian beam of ~ 60 mas FWHM. As in the case of the Gemini image, LR deconvolution was used because of its simpler use and greater speed. Since the NACO images are of much better quality (resolution and deepness) than the Gemini/SHARP data sets, deconvolution was not a critical issue in their case.

3. Positions and proper motions

The elaborate processing of the imaging data provided us with 12 final maps with resolutions between 60 to 130 mas FWHM for the epochs between 1992 and 2002 (no map for 1993, two maps for the 1996, 2000, and 2002 epochs each). These maps show the global evolution of the Sgr A* central cluster. Source confusion in this cluster is high, so that because of the high proper motions a star may “merge” at some epoch with another one and “reappear” at some later epoch. With a baseline that is long enough, it is possible to disentangle these stellar motions. Source identification (and reidentification at a later epoch) is usually done “by eye”. In order to cross-check and support our “by eye” identifications, we implemented a largely automatized procedure that, given initial source positions and identifications at one epoch, identifies the selected sources and measures their positions in the maps of all other epochs.

Assuming constant relative fluxes of the stars, the appearance of the stellar cluster at different epochs results just from rearrangements of the stars. If the differences in the positions of the stars are not too large, which is e.g. the case for two maps from subsequent observing epochs, this rearrangement can be done automatically with a least squares fit (that also takes into account an offset in the overall flux and adapts the PSF FWHM to the respective images). To start the position finding algorithm, we measured the positions and relative fluxes of stars in the cluster in the NACO August 2002 image, the deepest and highest resolution image in our data set. From these initial estimates, a model image (using Gaussian PSFs) was created that was subsequently fit (in a least square sense) to the maps of the stellar cluster at the earlier epochs. Hence, the measured positions of the stars at one

observing epoch were used as initial estimates for the positions in the preceding epoch. 9 bright, isolated reference stars served for transforming the initial positions into the respective individual image frames with their unique rotation angles and different pixel scales.

We implemented the procedure described above in a series of IDL program codes and extracted the stellar positions in three steps. First, the brighter members of the cluster around Sgr A* were fitted and subtracted from the maps. The procedure was then repeated with fainter stars on the subtracted maps from step 1. In a third iteration final positions were obtained by taking the positions of the brighter and fainter stars measured in steps 1 and 2 for all epochs and fitting them simultaneously to the original maps of all epochs. With this final iteration, we tried to minimize the influence that sources very close to each other have on their mutual positions. Errors on the measured positions were determined by comparing the positions from the fitting procedure with centroid positions measured on the stars with two different apertures sizes and taking the maximum deviation of the centroid positions from the fitted position as an error estimate.

With the positions (in pixels) measured by the procedure described above, the offsets of the stars from Sgr A* in right ascension and declination were calculated by a second order transformation onto an astrometric frame using the positions and proper motions of 9 bright, isolated stars in our field of view from the Ott et al. (2003) list. This means that our astrometric system is ultimately established by the SiO maser astrometry defined by Reid et al. (2003). Errors of this transformation were estimated by taking the standard deviations of 9 measured positions, which we obtained by repeating the transformation with different subsets of 8 out of the nine stars. The transformation errors were added quadratically to the positional errors described above.

We determined stellar proper motion velocities by a linear least squares fit to the time dependent stellar positions. In a final step, we controlled the derived positions and proper motions by comparing model images created with the measured quantities to the observed images at each observing epoch. In a few cases, the automated procedure failed to disentangle the motions of stars that were at coincident positions at some epochs and of comparable magnitudes. In some other cases, very faint stars “merged” with bright stars at some epoch, but it could not be determined reliably when and where they “reappeared”. We rejected these sources with ambiguous proper motions from our list.

Based on the entire data set, we thus determined proper motions for 35 stars within 1.2'' of Sgr A*. The main limitation to our sample comes from the resolution of the SHARP/NTT data. We could measure the proper motion of an additional 11 stars based on the higher resolution Gemini 2000 and NACO August 2002 images. With only two position measurements, however, the velocities of these stars are subject to significantly larger errors.

As an additional cross-check of the measured stellar positions, we compared the time dependent positions of the stars S2 and S8 with the ones published by Ghez et al. (2000), who have used the 10m-class Keck telescope for a very similar proper motion study (see Figure 2). In order to take into account the repositioning of Sgr A* by Reid et al. (2003), we applied an offset of 0.040'' West and 0.009'' North to the Keck data that we calculated from the differences in the positions of S2 for the 1995 epoch. As can be seen in Figure 2, the two groups' results are in excellent agreement.

Our final list of stars with their magnitudes, their positions relative to Sgr A* in August 2002, and their proper motion velocities is given in Table 1. All velocities were calculated assuming a distance of 8 kpc to the Galactic Center (Reid 1993). An additional systematic error of the order $\sim 20 \text{ km s}^{-1}$ should be taken into account because of possible systematic errors of $\sim 0.003''$ in the stellar positions (see section 5). The photometry was calibrated by selecting suitable reference stars from the Ott et al. (2003) list. Magnitudes were measured by aperture photometry on the Lucy-Richardson deconvolved CONICA/NAOS image from August 2002, with errors estimated by choosing different aperture sizes. Figure 4 illustrates the measured stellar proper motions with velocity vectors superposed on a NACO 2002.4 map.

We identified 6 stars which were subject to significant acceleration (deviation from a linear trajectory $> 3\sigma$) and have marked them with an asterisk in Table 1. The proper motion velocities given for these stars for the 2002 epoch were derived from linear fits to subsets of the measured positions, i.e. to time spans that were short enough to approximate the motions of the stars by linear trajectories. Therefore, they are approximate estimates and should not be used for modeling.

As for the naming of some individual sources, S1 through S12 were named in earlier publications about the central cluster, e.g. Genzel et al. (1997). S12 was mentioned by Genzel et al. (1997) as a possible variable source and counterpart of Sgr A*. Ghez et al. (1998) detected this source as well, but excluded the possibility of it being a Sgr A* counterpart because of its large proper motion, which was inconsistent with the expected extremely low proper motion of Sgr A*. Also, the repositioning of Sgr A* by Reid et al. (2003) moved its location $\sim 50 \text{ mas}$ East of the position used by Genzel et al. (2000). With our new analysis, based on a much longer time line, we arrive at the following interpretation: S12 (Genzel et al. 1997) was coincident (at the level of the SHARP resolution) with a fainter source, S3, in the 1995 epoch. It passed the pericenter of its orbit at that time, moving at $> 1000 \text{ km/s}$. The proper motion of S12 was directed towards the north. In 1998 and 1999 it was located so close to the brighter source S2 that it could hardly be separated with the resolution of SHARP/NTT. S12 “reappeared” north of S2 in 2000. We dropped S3 from

our list because we could not determine an unambiguous proper motion for that source. We show maps for the epochs 1995.5, 1996.4, 1999.5, and 2000.5 in Figure 3. All stars labeled in these maps (except S3) were subject to significant accelerations as described below.

4. Accelerations

We found that 6 stars in our sample (S1, S2, S8, S12, S13, S14) show clear signs of nonlinear proper motion, 3 of which are well known candidates, i.e. S1, S2, and S8 (Ghez et al. 2000; Eckart et al. 2002; Schödel et al. 2002). We measured the accelerations of the five stars S1, S2, S8, S12, and S13 with parabolic fits to 3 different sections of their trajectories (in the cases of S2 and S12, sections of the orbits with small changes in acceleration). The sections were chosen such that the change of acceleration was negligible for each star. From the 3 fits, we calculated average accelerations, with corresponding average epochs and positions. They are listed in Table 2. In the case of S14 the data did not allow such a procedure because its orbit is seen almost edge on (see Figure 6).

In Figure 5 we show the corresponding acceleration vectors with their error cones, as determined from the averages of the three parabolic fits. The radio position of Sgr A* (Reid et al. 2003) lies within these error cones for S1, S2, S12, and S8, but not for S13. However, the latter star is one of the fainter sources in our sample and has been located very close to S1 between the 1997 and 2000 epochs, which might have deteriorated its measured positions. Its trajectory will become more precisely determined with future NACO observations. We therefore excluded S13 from the following analysis of the location of Sgr A*.

With the measured projected accelerations of S1, S2, S12, and S8, we used a maximum likelihood analysis similar to Eckart et al. (2002) to determine the position of the dark mass. We used the accelerations and errors calculated from the three individual parabolic fits to each star’s trajectory. The position of Sgr A* can be derived from the sum of the 12 resulting χ^2 maps (3 maps for S1, S2, S12, and S8, respectively). We find from this analysis that the most probable location of the dark mass is 7_{-11}^{+12} mas West and 3_{-20}^{+21} mas South of the radio position of Sgr A*. The confidence limits correspond to $\Delta\chi^2 = +1$ ($\sim 68\%$ probability).

Table 3 lists the enclosed projected masses as derived from the projected total accelerations. We list values for the inclination of the orbits of S1, S2, and S8 that were estimated by comparing the projected mass to an intrinsic black hole mass of $2.9 \pm 0.2 \times 10^6 M_\odot$ (see section 7.1). The high acceleration of S13 gives a too large enclosed mass and cannot be used for estimating the inclination. However, it suggests that its orbit must lie close to the plane of the sky. The enclosed mass determined for S12 with this method is also too high

and does not allow estimating the inclination of its orbital plane. S12 was close to bright sources, like S4, S1, and S2, most of the time, so it was in this case hard to find suitable orbital sections large enough for fitting well constrained parabolas to them.

5. Orbits

The gravitational potential in the central 0.5 pc is dominated by that of a point mass (Eckart & Genzel 1997; Genzel et al. 2000; Ghez et al. 2000; Eckart et al. 2002; Schödel et al. 2002). If we consider that the mass to light ratio within 0.55" of SgrA*, is comparable to that of the outer cluster ($M/L(2\mu m) = 2 \times M_{\odot}/L_{\odot}$), the stellar mass in this radius due to the stellar cusp will be $\sim 5000 M_{\odot}$ and the combined relativistic and Newtonian peri-astron shift of S2 is of the order ≤ 10 minutes of arc per year (Rubilar & Eckart 2001; Mouawad et al. 2003). It is therefore reasonable to analyze the motions of the stars in the Sgr A* cluster in terms of keplerian orbits. The four stars S1, S2, S12, and S14 passed through the pericenter of their orbits during the time span covered by our observations. In the case of the three stars S2, S12, and S14 sufficiently large sections of their orbits were observed in order to allow for a unique keplerian fit. As for S1, S8, and S13, unique fits were not possible, but we constrained their orbits, using the estimated inclinations from Table 2.

We calculated the orbital parameters by fitting keplerian orbits to the observed time-dependent positions in the plane of the sky. The “best” fit was determined in the least-squares sense. For this purpose, we built IDL program codes around the IDL MPFIT/MPCURVEFIT procedures. These procedures use the Levenberg-Marquardt technique to solve the least-squares problem for a given set of data points and for a given function.⁵ If a significant part of an orbit (of the order 50%) has been covered by observations, it is thus possible to determine its period, semi-major axis, time of pericenter passage, eccentricity, and the three angles of orientation, the inclination (except its sign), the angle of the line of nodes, and the angle from node to pericenter. This is based on the assumption that the proper motion of Sgr A* relative to the surrounding stars can be neglected. With additional spectroscopic information about line-of-sight velocities (which were not available for this work) one can also determine the sign of the inclination and the distance to the GC (Salim & Gould 1999; Eisenhauer et al. 2003).

We let the initial estimates vary over an appropriately large range in parameter space in order to ensure finding the global minimum of the fit. In the cases of S2, S12, and S14, the

⁵The MPFIT program library has been written by Craig Markwardt and is publicly available at <http://cow.physics.wisc.edu/~craigm/idl/idl.html>

initial estimates could be found fairly well from ellipses fitted to their projected trajectories. In the cases of S1, S8, and S13, where unique fits were not possible, we calculated their orbital parameters for three different inclination angles, which were held fixed in the fitting procedure.

All results for the orbital parameters are listed in Table 5. Only in the case of S2 the position of Sgr A* was treated as a free parameter. For the other orbits astrometric errors of the parameters must be taken into account additionally because of the error in the radio position of Sgr A*. They are of the same order as the fitting errors. The measured time dependent positions of the stars and their projected orbits as determined by the fits are plotted in Figure 6. Ghez et al. (2003a) have published orbital solutions for all the stars described below, which appear to be in good agreement with our results. As for terminology, they name the sources S0-1 (S1), S0-2 (S2), S0-4 (S8), S0-16 (S14), S0-19 (S12) and S0-20 (S13).

- **S2:** The orbit of S2 has already been reported by Schödel et al. (2002). Since S2 passed through pericenter early in 2002, the measurements from that epoch are particularly important for constraining its orbit. For the analysis of S2, we therefore decided to include in the case of S2 additional imaging data made with NACO at the VLT in 2002, i.e. data for the epochs 2002.25, 2002.33, and 2002.58 (Schödel et al. 2002).

The NACO AO observations at each epoch provided series of usually several tens of individual exposures of the GC stellar cluster. Schödel et al. (2002) reported S2 positions for the NACO data based on the final co-added image for each observing epoch. In this work, we chose a slightly different approach: S2 is easily identified in individual exposures without having to apply any post-processing. Therefore, we measured its position at each NACO observing epoch by using all available individual exposures. We took the resulting average position, with the standard deviation of the individual measurements as an error estimate. These errors are generally lower than the conservatively estimated errors of Schödel et al. (2002).

To estimate the systematic error of our SHARP positions, we compared them with the positions of Schödel et al. (2002), which are taken from Ott et al. (2003), and are based on a different data reduction and analysis technique. From this comparison we estimated a potential ~ 3 mas systematic error on the SHARP positions. We added this error to our measured positions. The systematic error in position estimated from this “cross-calibration” leads to an additional systematic error of the order 20 km/s in the proper motion velocities listed in Table 1.

Our analysis of the orbit of S2 is distinct in one other point from Schödel et al. (2002): We treated the position of Sgr A* as a free parameter when fitting the orbit of S2.

The resulting orbital parameters and their formal errors (resulting from an analysis of the covariance matrix) are listed in column 1 of Table 5. We find a black hole mass of $3.3 \pm 0.7 \times 10^6 M_\odot$. The position of the focus of the orbit is 2.0 ± 2.4 mas East and 2.7 ± 4.5 mas South of the nominal radio position. This means that the position of the acceleration center lies well within the 1σ error circle of the radio position of Sgr A*.

Figure 7 compares our data and orbital solution for S2 to the orbit and positions published by Schödel et al. (2002). We find an excellent agreement within the errors. Only the 1992 position seems to be subject to a larger deviation. We attribute this to the chip readout pattern in the 1992 data (see section 2.1). We also found that weighting of the data is a crucial issue in fitting keplerian orbits. Therefore, we compare the orbital parameters for the two cases of normal and equal weighting in Table 4. The results agree very well within the errors and with the values of Ghez et al. (2003). However, since the radio position of Sgr A* is only known to 10 mas, the offsets of the focus determined by the two groups are not directly comparable. The important point is that both groups find that the center of attraction is offset just a few mas from the radio position of Sgr A* determined by Reid et al. (2003).

- **S12:** S12 passed through pericenter in 1995.3. It is a fairly weak source and has been close to brighter sources, like S2 and S4, at most of the observing epochs. It passed between S1 and S2 in 1996/97. In 1998 it was almost coincident with S2 and only “reappeared” in 1999/2000 north of S2 (see Figure 3). For these reasons, it was not realized earlier that it was a star that had passed through pericenter. The result of the orbital fit tells us that it must have been almost coincident with S4 in the 1992 epoch. Photometric measurements support this assumption because S4 is 0.5 mag brighter in the 1992 image, consistent with the sum of the fluxes of S4 and S12. However, we did not use the 1992 position for the orbital fit. The black hole mass determined from the orbit of S12 is $3.5 \pm 2.5 \times 10^6 M_\odot$. This includes the astrometric error (The focus of the ellipse was not fitted in the case of S12).
- **S14:** The orbit of this star was first identified by (Ghez et al. 2003a), who named this source S0-16. The quality of our data made the orbit of S14 difficult to determine. We could only measure reliable positions between the 1998 and 2002 epochs. When fitting the orbit, we obtained two formal solutions, but disregarded the one that resulted in an unrealistic black hole mass of $> 10^7 M_\odot$. S14 is a remarkable source because its orbit is extremely eccentric and is seen almost edge on. The closest point of approach of this star to the black hole is less than half a light day, i.e. in principle, it poses even stronger constraints on the central mass distribution than S2. Unfortunately, we could only determine a very crude enclosed mass estimate of $6.4 \times 10^6 M_\odot$ with the error of the same order as this value.

- **S1, S8, S13:** The orbits of these stars cannot be determined with a unique solution yet. However, in order to gain a general idea of their orbital parameters we fitted the orbits with the inclination angle held fixed at different values, using as an orientation the inclination estimates of Table 3. The results for the three stars are given in Table 5, with superscripts and subscripts being the best fitting values for the respective (superscript or subscript) inclination angles.

5.1. Anisotropy

With our new proper motion data, we looked for possible anisotropy in the velocity structure of the Sgr A* stellar cluster, using $\gamma_{TR} = (v_T^2 - v_R^2)/v^2$ as anisotropy estimator, where v is the proper motion velocity of a star, with v_T and v_R its projected tangential and radial components. A value of +1 signifies projected tangential motion, -1 projected radial motion of a star. The properties of the anisotropy parameter γ_{TR} are discussed in detail in Genzel et al. (2000). They show that an intrinsic three-dimensional radial/tangential anisotropy will be reflected in the two-dimensional anisotropy estimator γ_{TR} .

The errors of the proper motions that are based solely on the Gemini 2000 and the NACO August 2002 data are too large for this analysis and were therefore not used. In Figure 8 we have plotted γ_{TR} against the projected distance from Sgr A* (epoch 2002.7) for the remaining stars from Table 1. In Figure 9 we show histograms of γ_{TR} for stars within $0.6''$ (dotted lines), $1''$ (straight lines), and $1.2''$ (dashed lines) of Sgr A*. Since the stars changed their positions during the time span covered by the observations, we calculated the anisotropy parameter for the 2002.5 (lower panel) and for the 1995.5 (upper panel) epochs. In all cases, the number of stars on radial orbits is $2 - 3\sigma$ (assuming Poisson errors) above the number of stars on projected tangential orbits (cf. Figure 8 of Genzel et al. 2000, who show histograms of γ_{TR} for clusters with varying intrinsic anisotropy).

From the projected radial velocity dispersions and the ratio of projected tangential to radial velocity dispersions listed in Table 6 (see section 7.1), we can estimate the anisotropy of the stellar cluster with the aid of equation (10) of Genzel et al. (2000):

$$\langle\beta\rangle = 1 - \langle\sigma_t^2\rangle/\langle\sigma_r^2\rangle = 3(\langle\sigma_R^2\rangle - \langle\sigma_T^2\rangle)/(3\langle\sigma_R^2\rangle - \langle\sigma_T^2\rangle) \quad (1)$$

Averaging the results of the 4 lists in Table 6, we find $\langle\beta\rangle = 0.5 \pm 0.2$. Of course, this value has to be taken with a certain caution. While the value of the anisotropy agrees very well for three of the lists, we obtain a value of $\beta \sim 0$ in one out of the four cases. Genzel et al. (2000) also showed that a measurement of β from a small sample of stars can easily be skewed towards positive values. However, their simulations showed that the probability of

measuring $\beta \geq 0.5$ is as low as 25% for a sample of ≥ 30 stars out of intrinsically isotropic or tangentially anisotropic clusters (see their Figure 10).

Additionally, we checked whether any sky-projected overall rotation of the stars can be detected. Like Genzel et al. (2003) we used the normalized angular momentum $J_z/J_z(max) = (xv_y - yv_x)/pv_p$, where x and y are the offsets from Sgr A* in R.A. and Decl., v_x and v_y the corresponding velocity components, and p and v_p the projected distance from Sgr A* and the absolute value of the proper motion velocity. We show the plot of this parameter against the projected distance in Figure 10, for the epoch 2002.7 (plotting the parameter for another epoch does not introduce any significant change). We find no significant projected overall rotation of the cluster.

6. Limits on the emission of Sgr A*

All of the brighter ($K \geq 15.5$) sources that can be found in our maps at some epochs at distances $< 0.1''$ from Sgr A* are stars with known proper motions, like S1, S2, or S12. Although fainter sources ($K \leq 16$) can be found within $0.1''$ mas of the location of Sgr A* at some epochs as well, they are at least ~ 30 mas offset from the exact radio position. Hence, with the data base used for this work, we find no clear sign of a stationary or variable (≥ 0.5 mag) source at the position of Sgr A*.

Since we have combined the best speckle frames taken during entire observing runs (which comprised usually several days) for our present data analysis, this statement does only refer to variability on the scale of at least several hours to several days. As for shorter term variability, we did not note any unusual activity at the position of Sgr A* when selecting thousands of 0.5 s speckle frames by eye as described in section 2.1. However, in order to be clearly seen in a single SHARP speckle frame, a source must have a K magnitude of ~ 13.5 or brighter.

We estimated a simple limit on the average emission of Sgr A*. From aperture photometry with an aperture of ~ 50 mas and calibration relative to stars in the cluster we determined a conservative upper limit of $K > 16$ for the emission of Sgr A* in the epochs before 2000.5 (At that epoch the bright source S2 moved to within $\sim 0.05''$ of Sgr A*). Using the Galactic Center extinction law of Raab (2002) ($A(K) = 3.2$), we derive an upper limit of < 5 mJy on the emission from Sgr A*. This is of the same order as the results of Hornstein et al. (2002) and Genzel et al. (2003).

7. Summary and Discussion

7.1. The central dark mass

With the proper motions from Table 1 we calculated the enclosed mass with the Leonard-Merritt (LM, Leonard & Merritt 1989) mass estimator. For this purpose we compiled various lists of stellar positions and velocities. We created a long list (LL) with all sources from Table 1 and a short list (SL) that excludes the larger error proper motions determined just from the Gemini/NACO images. Additionally, we measured the projected velocities of the accelerated stars at two different epochs in order to take into account the influence of their varying velocities. We thus obtained 4 lists (SL1, SL2, LL1, LL2). Table 6 lists the calculated values of the enclosed mass, of the radial velocity dispersion, and of the ratio between the projected radial and tangential velocity dispersions for all 4 cases.

Genzel et al. (2000) showed that the LM mass estimate M_{LM} differs from the intrinsic mass M_0 of the central object depending on the anisotropy parameter β and the power-law slope of the central stellar cluster. This is because the LM mass estimate assumes that we have access to the full radial extent of the stellar cluster, which is not the case for our data set. From Figure 14 of Genzel et al. (2000) we estimate that $0.85 < M_{LM}/M_0 < 1.0$ for $0 < \beta < 0.5$ and a central density slope of $\alpha \approx 1.4$ (Genzel et al. 2003). Taking into account this range of the correction factor, we estimate a central mass of $3.4 \pm 0.5 \times 10^6 M_\odot$ from the weighted average of the LM mass estimates in Table 6. This is fully consistent with the value for the dark mass obtained from the orbit of S2.

Figure 11 is a plot of the measured enclosed mass against distance from Sgr A*, in close analogy to Figure 17 of Genzel et al. (2000) and Figure 3 of Schödel et al. (2002). The main differences to Schödel et al. (2002) are: (1) The error of the mass estimate from the orbit of S2 has been reduced by taking the position of the orbital focus explicitly into account. (2) The innermost LM mass estimate was based on the Ott et al. (2003) data in Schödel et al. (2002). It has been replaced by the LM mass estimate from the present work, which is based on more data in the region within $\sim 1''$ of Sgr A*. (3) The LM mass estimates in Figure 3 of Schödel et al. (2002) and Figure 17 of Genzel et al. (2000) were corrected downward by 5-10% because they assumed a power-law slope of $\alpha = 1.8$ for the inner stellar cluster. Now we use a power-law slope of $\alpha \approx 1.4$ (Genzel et al. 2003). This means that the LM mass estimates were previously underestimated by $\sim 10\%$.

Fitting a model composed of a point mass plus the visible stellar cluster with a core radius of 0.34 pc and a power-law slope of $\alpha = 1.8$ to the data gives a value of $2.9 \pm 0.2 \times 10^6 M_\odot$ for the central dark mass. This agrees within the errors with the LM mass estimate of the innermost stars and with the masses calculated from the orbital parameters of S2 and S12.

The values for the point mass given by Chakrabarty & Saha (2001) and Ghez et al. (1998) are systematically lower than the other estimates. If we disregard them in our analysis, we obtain a central mass of $3.1 \pm 0.2 \times 10^6 M_\odot$. In order to provide an overview over the different mass estimates, we have compiled some of them in Table 7. From their analysis of the orbit of S2, Ghez et al. (2003) measured the currently highest value of $4.1 \pm 0.6 \times 10^6 M_\odot$. It is the most extreme value, but could for example be realized if the central cluster were isotropic and its power-law index $\alpha \approx 1.3$ (see Figure 14 of Genzel et al. (2000)).

The mass of Sgr A* can also be constrained via its proper motion measured by radio astronomical observations. Reid et al. (2003a) find an upper limit of 8 kms^{-1} for the intrinsic proper motion of Sgr A*. Following their argument, we can apply equipartition of momentum to the case that the black hole is perturbed by close passages of stars. For S2, with a mass of $\approx 15 M_\odot$ and a velocity of $\approx 7000 \text{ kms}^{-1}$ at pericenter, we find a lower limit of $13 \times 10^3 M_\odot$. Dorband, Hemsendorf & Merritt (2003) model the Brownian motion that a supermassive black hole would have embedded in the stellar cluster at the center of the Milky Way. From their equation (73) we calculate a minimum mass of Sgr A* of $7.5 \times 10^3 M_\odot$ with the above proper motion constraint. Carrying the argument a bit further, we can interpret the upper limits on the size of Sgr A* at millimeter wavelengths as its half mass diameter. Assuming a half mass radius of $r_h \leq 0.1 \text{ mas}$ (Doeleman et al. 2001; Rogers et al. 1994; Melia & Falcke 2001) we obtain with the above mass estimates

$$\rho_{SgrA*} \geq \frac{7.5 \times 10^3 M_\odot / 2}{(4\pi/3)r_h^3} > 3 \times 10^{19} M_\odot \text{pc}^{-3} \quad (2)$$

Figure 12 is a summary of the lower limits on the density of the central dark mass obtained by different analyses. Considering our data, S2 places currently the tightest constraints on the central mass distribution. Although S14 approaches the dynamical center even closer, our data allow not to constrain its orbit with the necessary precision. The upper limit on the proper motion of Sgr A* relative to the surrounding star cluster gives the overall highest mass density constraint. If we assume a Plummer model cluster of dark astrophysical objects instead of a central point mass, its central density must exceed $2.2 \times 10^{17} M_\odot \text{pc}^{-3}$ as shown in Figure 11. The lifetime of such a cluster is limited to less $< 10^5$ years (Maoz 1998). A single fermion ball model that explains all the observed central dark mass concentrations at the centers of galaxies can also be excluded (Schödel et al. 2002). Considering that a boson star (Torres et al. 2000) should eventually collapse to a black hole through accretion of the abundant gas and dust in the GC, we conclude that current models and measurements compellingly suggest the presence of a supermassive black hole at the center of the Milky Way. As for a tight (< 10 light hours separation) binary black hole with similar masses of its two components, it would coalesce by gravitational radiation within a few hundred years (B.F. Schutz 2003, private communication).

7.2. Anisotropy of the central cluster?

We used the measured projected stellar velocities and the anisotropy estimator $\gamma_{TR} = (v_T^2 - v_R^2)/v^2$ to look for signs of anisotropy of the stellar cluster in the immediate vicinity of Sgr A*. We found a predominance of $\gamma_{TR} = -1$ on the $2 - 3\sigma$ level. This is of moderate statistical significance because of the small number of stars, but it is a stable result as to variation in epoch and in the size of the examined region around Sgr A*. The possible radial anisotropy appears to become more significant with shorter projected distances from the central black hole. No sign of a significant projected overall rotation is detected.

Genzel et al. (2000) based their claim of radial anisotropy in the inner $0.8''$ near Sgr A* on the absence of stars with $\gamma_{TR} = +1$. Although we now find some stars with $\gamma_{TR} = +1$ in our new proper motion data, this does not contradict a possible radial anisotropy. As Genzel et al. (2000) show, the distribution of γ_{TR} is always bimodal, so even in the case of radial anisotropy we expect some stars with $\gamma_{TR} = +1$. Hence, we feel that our analysis provides sufficient evidence for radial anisotropy of the sources brighter than $K \sim 16$. Whether this holds for the fainter sources as well, must be checked with the upcoming deep AO observations (see section 7.5). We suggest the following tests of anisotropy:

- The most obvious approach to the problem is measuring the proper motions of a greater number of stars. Observations with NACO at the VLT will provide such data on the fainter stars in the Sgr A* cluster within the next few years. We expect that the number of measured proper motions within $1''$ of Sgr A* will be augmented by a factor of 2 to 3.
- An alternative method to test the isotropy/anisotropy of the central stellar cluster is the eccentricity of stellar orbits: In a spherical system of test particles orbiting a point mass we expect that the number of particles with eccentricities in the range $(e, e + de)$ is proportional to ede (Binney and Tremaine, p. 282, problem 4-22). We show the corresponding cumulative distribution function in Figure 13. It is skewed towards high eccentricities: 75% of the stars have $e > 0.5$, 19% have $e > 0.9$ and 10% have $e > 0.95$. In the case of radial anisotropy, we expect even more stars on highly eccentric orbits because stars with specific energies E in an interval $(E, E + dE)$ would have a lower average angular momentum than in the isotropic case.

We included the eccentricities of the 6 orbits examined in section 5 into Figure 13. All points lie to the right and below the theoretical curve. This might be a hint that there are indeed more highly eccentric stellar orbits than in the isotropic case *if* there is no bias to detect preferentially orbits with high eccentricities. When examining such a possible bias in section 7.3, we find that eccentricities $e > 0.9$ could be subjected

to such a bias. However, the number of measured eccentricities is still too low for a conclusive test, but this method might provide a useful for future observations.

- In principle, the anisotropy of the central stellar cluster can also be measured by comparing the mass of the central black hole as determined from LM mass estimates to the mass determined from keplerian orbital fits.

Genzel et al. (2000) showed that the ratio between the true mass of the black hole at the center of the cluster and its LM mass estimator depends on both the power-law exponent α of the density of the central cluster and on its anisotropy parameter β (see their Figure 14). If one assumes the validity of keplerian orbits near Sgr A*, it is thus possible to determine β by comparing sufficiently precise mass measurements from individual orbits and LM mass estimators from analyses of sufficiently large proper motion samples. At the moment, the errors on the involved parameters still allow for a range of $0 \leq \beta \leq 0.5$. Future measurements, however, should set tighter limits.

With densities of the order 10^7 to $10^8 \text{ M}_{\odot} \text{pc}^{-3}$ in the central arcsecond (Genzel et al. 2003), two-body interactions should be comparably frequent and the relaxation time is less than 10^8 yr . In this case we would expect to observe an isotropic velocity field. There is a possibility that only the brighter, possibly young stellar component is unrelaxed and is characterised by radial anisotropy. It is clear that we need a larger and deeper proper motion data base before we can definitely exclude isotropy of the overall cluster. But should the radial anisotropy indeed be proven to be true, theoretical and modeling efforts will be needed to understand this property of the Sgr A* stellar cluster.

As a bottom line, we can say that the current data definitely exclude tangential anisotropy. Significant tangential anisotropy would be expected in systems with binary black holes (Gebhardt et al. 2002). Stars on highly eccentric orbits would be ejected or destroyed preferentially in such systems.

7.3. Biased detection of orbits?

In the previous section we saw that we could learn about the anisotropy characteristics of the dense stellar cluster surrounding Sgr A* from the measured eccentricities of the observed orbits. However, at this point the question arises whether there is a bias to detect preferentially circular or highly eccentric orbits.

When observing stellar proper motions/accelerations there is always a given lower limit for the detectable acceleration imposed by the limitations of the telescope, instrument, and

generally by the observing technique (e.g. time sampling). Consider two stars on keplerian orbits of equal energy (equal semi-major axis) around a black hole. The more eccentric of the two will spend less of its time near the black hole where its acceleration is detectable, and its eccentricity will therefore have a smaller probability of being measured. This effect biases the detected eccentricities towards smaller values. On the other hand, as long as $a < 2$ the number of stars per interval da increases with a (Appendix eq 4). These more numerous high- a stars can have large detectable accelerations only if their eccentricity is high enough to take them close to the black hole. This effect biases the detected eccentricities toward higher values. Thus, there are two competing trends that may introduce a bias to the measured distribution.

In order to obtain a rough quantitative estimate of the possible bias, we modeled families of keplerian orbits with fixed eccentricities and specific energies. We let their inclination angle i and the angle from node to pericenter ω (i.e. the rotation of the orbit in the plane of the orbit) vary on grids. ω was varied between 0 and 2π in equal steps of $\pi/6$, while $\sin(i)$ was varied in equal steps of 0.1 between -0.9 and 0.9 . For each of the individual orbits we calculated the fraction of the orbital period that the acceleration as seen projected onto the plane of the sky stayed above a given threshold value. We interpreted this fraction as the probability of detecting the given orbit. We chose as a detection threshold a minimum acceleration of 1 mas yr^{-2} , a value slightly lower than the lowest detected acceleration in our data sample (star S8). By averaging the probabilities over all angles i and ω , we obtained the overall detection probabilities for orbits with a given semimajor axis a and a given eccentricity e . We assumed an isotropic cluster and that the probability distribution function for e was independent of a . We assumed a time sampling of two observations per year.

That leaves creating an adequate distribution of semimajor axes. We chose a minimum semimajor axis corresponding to an orbital period of ~ 5 yr, which we consider a realistic value for our data sample. The upper limit for the distribution of semimajor axes is chosen to be 1 pc, roughly the distance over which the black hole dominates over the mass of the stellar cluster. The energy distribution function near a massive black hole has the form

$$f(\epsilon) = A\epsilon^p \quad n_* \propto r^{-3/2-p} \quad p = \frac{M}{4M_2} \quad (3)$$

if the stellar population consists of a spectrum of masses $M_1 < M < M_2$, where $\epsilon = -v^2/2 + GM_{BH}/r$ is the specific energy of the star and $f_M \equiv 0$ for $\epsilon < 0$ (Bahcall & Wolf 1977; see also Appendix A). n_* is the stellar number density. The distribution function of semimajor axes $n(a)$ for a given cusp model is then $n(a) \propto a^{1/2-p}$ (see appendix A). We created distributions of semimajor axes (1000 values of a sampled according to $n(a)$ between its minimum and maximum values) corresponding to isotropic power-law stellar cusps with

exponents α of -1.0 , -1.5 , and -2.0 . In the case of the Milky Way black hole the stellar density is approximately $n_* \propto r^{-3/2}$ (Genzel et al. 2003).

Figure 14 shows the probabilities of detecting orbits with a given e and a for the case of a $n \propto -1.5$ cusp. We only plotted the curves for orbits with $100 \text{ mpc} \gtrsim a$ because the plot would get extremely crowded at large semimajor axes and because the probabilities for large a are extremely low. For small a , the detection probability is large for all e , while at intermediate a , there is a bias towards less eccentric orbits. This bias turns over at large semimajor axes, when stellar accelerations can only be observed near the pericenter of highly eccentric orbits. However, for orbits with large a , detection probabilities are extremely low.

By averaging over all semimajor axes we obtained the overall detection bias of orbits with a given eccentricity in a given isotropic cusp model. The results are plotted in Figure 15. The exact values of the probabilities depend on the modelling parameters (e.g. the number of steps when creating the distribution of semimajor axes). However, we are only concerned with the relative probabilities. In the model with $\alpha = -2.0$ the stars are most concentrated toward the center and therefore the overall probabilities of detecting orbits are highest. In this case, there is no significant overall detection bias for any eccentricity. At the other extreme, in case of $\alpha = -1.0$, there is a bias factor of > 2 for highly eccentric orbits compared to circular orbits. This corresponds to our expectation that the relative weight of more circular orbits should decrease with a decreasing concentration of the cluster. The case of $\alpha = -1.5$, which is closest to the case of the GC stellar cusp, shows some bias toward high eccentricities. However, this bias is modest (factor $1.5 - 2$). Basically, it only affects significantly extreme eccentricities of $e > 0.9$.

With our modeling we wanted to provide a general idea of the possible biases involved in detecting stellar orbits around Sgr A*. As for the eccentricities of the stellar orbits found in the present work, out of the six stars two stars, i.e. S1 and S8, have semimajor axes in the regime where circular orbits are only detected with low probabilities. As for the orbits of the remaining four stars, they have semimajor axes that would favour the detection of more circular orbits. So there might be a bias on our sample, but the small number of orbits is not sufficient for a conclusive test.

7.4. No detection of a NIR counterpart of Sgr A*

We measured a conservative limit of 5 mJy on the dereddened emission of Sgr A* at $2.2\mu\text{m}$, in agreement with similar measurements (Hornstein et al. 2002; Genzel et al. 2003). We found no evidence for a varying and/or stationary source at the position of Sgr A* in

our maps. However, this addresses only time scales of at least several hours to days. Also, no variability at the position of Sgr A* was found in the course of the “by eye” inspection of thousands of speckle frames for every observing epoch. However, this method, where we could have picked up variability on time scales of seconds up to ~ 10 minutes, is limited by the short 0.5 s single frame integration times to K fluxes of ~ 13.5 or brighter. As for Hornstein et al. (2002), they sampled their data into 3 hour periods and found no significant variability. Combined with our present work, that leaves open time scales from seconds to several tens of minutes, at K magnitudes fainter than ~ 13.5 .

In the light of the results of Genzel et al. (2003), who found the predicted stellar cusp around Sgr A*, it is worthwhile to point out that the probability of detecting a $K \leq 17$ star at a projected position of $< 0.1''$ from Sgr A* is close to one. With a number density of > 50 stars arcsec^{-2} at distances $< 0.5''$ (see Figure 7 of Genzel et al. (2003)), we find that the average distance between stars in the central region is $< 0.1''$, when only taking into account stars brighter than $K \sim 17$.

In fact, Figure 7 of Genzel et al. (2003) suggests that even with an 8m-class telescope, the confusion limit might be reached within $0.1''$ of Sgr A* in deep ($K \sim 19$) NIR imaging observations. Additionally, if a NIR source at the position of Sgr A* could be detected, one would still have to measure its proper motion and photometric properties over several epochs and/or perform spectroscopy or polarimetry in order to clarify its nature. Hence, detecting Sgr A* in the NIR seems to be a difficult task.

However, current models of the accretion flow predict that the infrared emission comes from the tail of the non-thermal radio/submm emission, and not from a hot, thermal accretion disk (Markoff et al. 2001; Liu & Melia 2002). Therefore, attempts to detect Sgr A* at longer wavelengths, where the emission from hot stars is also significantly lower, seem more promising and will provide tighter constraints on the emission models.

7.5. Outlook

The stellar cusp in the immediate vicinity of Sgr A* provides the opportunity to study the interactions between its components and the central supermassive black hole on a level of detail that will never be achievable in other galaxies. It poses a number of intriguing astrophysical problems, such as its possible radial anisotropy and the theoretically unexpected presence of young, early-type stars (Ghez et al. 2003; Genzel et al. 2003). Observations in the next years will enable us to examine the Sgr A* cluster in unprecedented detail and hopefully solve some of its enigmas.

In the H-band, NACO at the VLT provides images with a resolution ~ 3 times higher than SHARP/NTT, reaching of the order 3 magnitudes deeper. In Figure 16, we show a Lucy-Richardson deconvolved NACO H-band image (reconvolved with a gaussian beam of FWHM ~ 40 mas) of 1500 s total integration time. We have counted “by eye” ~ 90 stellar sources with magnitudes $H \leq 18$ within $1''$ of Sgr A*. There are of the order 20 stars within $0.5''$ of Sgr A* with poorly known or unknown proper motions. All of these sources are candidates for measuring accelerations and constraining the properties of stellar orbits near the supermassive black hole. We will thus be able to build a proper motion data base with much improved statistics. It will then be possible to settle the question of the isotropy/anisotropy of the central stellar cluster under consideration of the faint component.

We expect also to determine stellar orbits with a much higher precision and to detect several faint stars with orbital periods of the order 10-20 years. This will allow to locate the center of acceleration to within < 1 mas and to measure the mass of the black hole precisely and without the assumptions involved in statistical methods. Measuring the radial velocity of the orbiting stars allows a precise determination of the distance to the Galactic Center (Salim & Gould 1999; Ghez et al. 2003; Eisenhauer et al. 2003). We expect that stars will be found orbiting Sgr A* with velocities $\geq 0.1 \times c$, approaching the relativistic regime.

Spectroscopy of sources in the dense stellar cluster with AO slit spectroscopy (Ghez et al. 2003) and AO integral-field units (SPIFFI/SINFONI at the VLT) will help us understand the nature of the stars near the black hole and their three-dimensional velocity and space distribution. Finally, imaging and polarimetric observations at longer wavelengths will help constrain the parameters of the accretion flow onto Sgr A*.

We like to thank the ESO NTT team for their help and support during ten years of observations with the SHARP guest instrument.

We thank the NAOS and CONICA team members for their hard work, as well as the staff of Paranal and the Garching Data Management Division for their support during the commissioning and science verification of NACO.

We thank Andrea Ghez of UCLA for helpful discussions and exchange of opinions on the stellar orbits, especially for understanding the orbit of S14/S0-16.

Rainer Schödel thanks William D. Vacca for his great help on fitting techniques.

TA is supported by GIF grant 2044/01, Minerva grant 8484, and a New Faculty grant by Sir H. Djangoly, CBE, of London, UK.

Based in part on observations obtained at the Gemini Observatory, which is operated by

the Association of Universities for Research in Astronomy, Inc., under a cooperative agreement with the NSF on behalf of the Gemini partnership: the National Science Foundation (United States), the Particle Physics and Astronomy Research Council (United Kingdom), the National Research Council (Canada), CONICYT (Chile), the Australian Research Council (Australia), CNPq (Brazil) and CONICET (Argentina).

A. The spherically symmetric power-law cusp

We present here for convenience a self contained summary of some properties of the distribution function (DF) of a spherically symmetric system, and apply them to a power-law cusp and keplerian orbits.

A.1. Isotropic velocity field

The DF $f(\varepsilon)$ of a system with an isotropic velocity field is a function of the specific energy only, $\varepsilon \equiv -v^2/2 + \psi(r)$, where $\psi \equiv -\phi$ and ϕ is the gravitational potential (f has units of $x^{-3}v^{-3}$; $f(\varepsilon) = 0$ for $\varepsilon \leq 0$). The space density distribution, $n(r) \equiv \int f(\varepsilon)d^3v$ (in units of x^{-3}), is

$$n(r) = 4\pi \int_0^{\sqrt{2\psi(r)}} f(\varepsilon)v^2dv = 4\pi \int_0^{\psi(r)} f(\varepsilon)\sqrt{2(\psi - \varepsilon)}d\varepsilon, \quad (\text{A1})$$

where the last step is made with the variable transformation $d\varepsilon = -v dv$, and $v = \sqrt{2(\psi - \varepsilon)}$.

For a power-law DF, $f(\varepsilon) = A\varepsilon^p$,

$$n(r) = (2\pi)^{3/2} \frac{\Gamma(1+p)}{\Gamma(5/2+p)} A\psi(r)^{3/2+p}. \quad (\text{A2})$$

Very near the black hole the orbits are keplerian to a good approximation, $\psi = Gm/r$, and therefore $n(r) \propto r^{-3/2-p}$.

The distribution of specific energy is $n(\varepsilon) \equiv \int f(\varepsilon')\delta(\varepsilon' - \varepsilon)d^3x d^3v$ (in units of v^{-2}), where δ is the Dirac delta function (in units of the inverse of its argument). Using the property $\delta(h(x)) = \delta(x - x_0)/|dh/dx|$, where $h(x_0) = 0$, and performing first the integration over velocities, one obtains for keplerian orbits ($a = Gm/2\varepsilon$)

$$n(\varepsilon) = (4\pi)^2 f(\varepsilon)\sqrt{Gm} \int_0^{2a} \sqrt{2/r - 1/ar^2} dr$$

$$\begin{aligned}
 &= \sqrt{2}\pi^3(Gm)^3 f(\varepsilon)\varepsilon^{-5/2} \\
 &= 2^{3-p}\pi^3(Gm)^{1/2+p}Aa^{5/2-p}.
 \end{aligned} \tag{A3}$$

The distribution of semi-major axes, $n(a)$ (in units of x^{-1}) is therefore

$$n(a) = |d\varepsilon/da| n(\varepsilon) = 2^{2-p}\pi^3(Gm)^{3/2+p}Aa^{1/2-p}. \tag{A4}$$

The distribution of eccentricities in a spherically symmetric distribution of keplerian orbits with an isotropic velocity field is derived below (Eq. A8).

A.2. Anisotropic velocity field

In the general spherically symmetric case, the DF $f(\varepsilon, L)$ depends on both the specific energy $\varepsilon = -v_r^2/2 - L^2/2r^2 + \Psi$ and the magnitude of the specific angular momentum, $L^2 = (rv_t)^2$, where v_r and v_t are the radial and transverse components of the velocity relative to the radius vector.

In cylindrical coordinates $d^3v = 2\pi v_t dv_t dv_r$, and so substituting $v_t dv_t = LdL/r^2$, $dv_r = -d\varepsilon/v_r$ with an extra factor of 2 to account for both contributions from $\pm v_r$ to $d\varepsilon$, one obtains

$$d^3v = 4\pi L dL d\varepsilon /r^2 |v_r(\varepsilon, L, r)|. \tag{A5}$$

The distribution of specific energy and angular momentum, $n(\varepsilon, L)$ (in units of $x^{-1}v^{-3}$) is obtained by integrating $f(\varepsilon, L) 4\pi r^2 dr d^3v/d\varepsilon dL$ over the range (r_-, r_+) that is accessible with ε and L ,

$$\begin{aligned}
 n(\varepsilon, L) &= 16\pi^2 L f(\varepsilon, L) \int_{r_-}^{r_+} \frac{dr}{|v_r(\varepsilon, L, r)|} \\
 &= 8\pi^2 L f(\varepsilon, L) T_r(\varepsilon, L),
 \end{aligned} \tag{A6}$$

where T_r is the radial period and the integral expresses the contribution from each dr segment of the orbit, weighted by the time spent there.

For keplerian orbits $\varepsilon = GM/2a$, $L^2 = GMa(1 - e^2)$ and $T_r = P(\varepsilon) = \pi GM/\sqrt{2\varepsilon^3}$, and so $2L dL = -(GM)^2/(2\varepsilon)e de$. It then follows from Eq. (A6) that the distribution of specific energy and eccentricity (in units of v^{-2}) is (cf Cohn & Kulsrud 1978)

$$n(\varepsilon, e) = \left[2\sqrt{2}\pi^3(GM)^3 f(\varepsilon, L)\varepsilon^{-5/2} \right] e, \tag{A7}$$

It then follows that for keplerian orbits with *isotropic* velocities the distribution of eccentricities $n(e)$ (dimensionless) is (cf Binney & Tremaine 1987)

$$n(e) = \left[2\sqrt{2}\pi^3(GM)^3 \int f(\varepsilon)\varepsilon^{-5/2} d\varepsilon \right] e \propto e. \quad (\text{A8})$$

REFERENCES

- Alexander, T. 1999, *ApJ*, 527, 835
- Baganoff, F.K., Bautz, M.W., Brandt, W.N., Chartas, G., Feigelson, E.D., Garmire, G.P., Maeda, Y., Morris, M., Ricker, G.R., Townsley, L.K., & Walter, F. 2001, *Nature*, 413, 349
- Bahcall, J.N., & Tremaine, S. 1981, *ApJ*, 244, 805
- Bahcall, J.N., & Wolf, R. A. 1977, *ApJ*, 216, 883
- Binney, J., & Tremaine, S. 1987, *Galactic Dynamics* (Princeton: Princeton Univ. Press), p. 282
- Chakrabarty, D., & Saha, P. 2001, *AJ*, 122, 232
- Cohn, H. & Kulsrud, R. M. 1978, *ApJ*, 226, 1087
- Doeleman, S. S., Shen, Z.-Q., Rogers, A. E. E., Bower, G. C., Wright, M. C. H., Zhao, J. H., Backer, D. C., Crowley, J. W., Freund, R. W., Ho, P. T. P., Lo, K. Y., Woody, D. P. 2001, *AJ*, 121, 2610
- Dorband, E. N., Hemsendorf, M., & Merritt, D. 2003, *J. Computational Phys.*, 185, 484
- Eckart, A., & Genzel, R. 1997, *MNRAS*, 284, 576
- Eckart, A., Genzel, R., Ott, T., & Schödel, R. 2002, *MNRAS*, 331, 917
- Eisenhauer, F., Schödel, R., Genzel, R., Ott, T., Tecza, M., Abuter, R., Eckart, A., & Alexander, A. 2003, submitted to *ApJ*
- Gebhardt, K., Richstone, D., Tremaine, S., Lauer, T. R., Bender, R., et al. 2003, *ApJ*, 583, 92
- Genzel, R., & Townes, C.H. 1987, *ARA&A*, 25, 377
- Genzel, R., Thatte, N., Krabbe, A., Kroker, H., & Tacconi-Garman, L. E. 1996, *ApJ*, 472, 153

- Genzel, R., Eckart, A., Ott, T., & Eisenhauer, F., 1997, MNRAS, 291, 219
- Genzel, R., Pichon, C., Eckart, A., Gerhard, O. E., & Ott, T. 2000, MNRAS, 317, 348
- Genzel, R., Hofmann, R., Lehnert, M., Ott, T., Schödel, R., Alexander, T., Sternberg, A., Lenzen, R., Lacombe, F., Rouan, D., Zoccali, M., & Renzini, A. 2003, ApJ, in press
- Ghez, A., Klein, B. L., Morris, M., & Becklin, E. E. 1998, ApJ, 509, 678
- Ghez, A., Morris, M., Becklin, E. E., Tanner, A., & Kremenek, T. 2000, Nature, 407, 349
- Ghez, A., Duchêne, G., Matthews, K., Hornstein, S.D., Tanner, A., Larkin, J., Morris, M., Becklin, E. E., Salim, S., Kremenek, K., Thompson, D., Soifer, B.T., Neugebauer, G., & McLean, I. 2003, ApJ, 586, L127
- Ghez, A. M., Becklin, E., Duchêne, G., Hornstein, S., Morris, M., Salim, S., & Tanner, A. 2003, Astron. Nachr., Vol. 324, No. S1, Special Supplement "The central 300 parsecs of the Milky Way", Eds. A. Cotera, H. Falcke, T. R. Geballe, S. Markoff
- Hofmann, R., Brandl, B., Eckart, A., Eisenhauer, F., Tacconi-Garman, L. E., in Proc. SPIE 1995, 2475, 192
- Hornstein, S. D., Ghez, A. M., Tanner, A., Morris, M., Becklin, E. E., Wizinowich, P. 2002, ApJ, 577, L9
- Jeffries, S. M., & Christou, J. C. 1993, ApJ, 415, 862
- Kormendy, J. 2001, RevMexAA, 10, 69
- Krichbaum, T. P., Graham, D. A., Witzel, A., Greve, A., Wink, J. E., Grewing, M., Colomer, F., de Vicente, P., Gomez-Gonzalez, J., Baudry, A., Zensus, J. A. 1998, A&A, 335, 106
- Lenzen, R., Hofmann, R., Bizenberger, P., & Tusche, A. 1998, in Proc. SPIE IR Astr. Instr. (ed. A.M. Fowler), 3354, 606
- Leonard, P.J.T., & Merritt, D. 1989, ApJ, 339, 195
- Liu, S. & Melia, F. 2002, ApJ, 566, L77
- Melia, F., & Falcke, H. 2001, ARA&A, 39, 309

- Mouawad, N., Eckart, A., Pfalzner, S., Straubmeier, C., Spurzem, R., Genzel, R., Ott, T., & Schödel, R., *Astron. Nachr.*, Vol. 324, No. S1 (2003), Special Supplement "The central 300 parsecs of the Milky Way", Eds. A. Cotera, H. Falcke, T. R. Geballe, S. Markoff
- Mouawad, N., Eckart, A., et al. 2003, in preparation
- Maoz, E. 1998, *ApJ*, 494, L181
- Markoff, S., Falcke, H., Yuan, F., Biermann, P.L. 2001, *A&A*, 379, L13
- Munyaneza, F. & Viollier R.D. 2002, *ApJ*, 564, 274
- Ott, T., Genzel, R., Schödel, R., & Eckart, A. 2003, in preparation
- Ott, T., Schödel, R., Genzel, R., Eckart, A., Lacombe, F., et al. 2003, *The Messenger*, 111, 1
- Raab, W. 2002, Ph.D. Thesis, Ludwig-Maximilians-Universität, München
- Reid, M. 1993, *AnnRevAA*, 31, 345
- Reid, M., Readhead, A.C.S., Vermeulen R.C., & Treuhaft, R.N. 1999, *ApJ*, 524, 816
- Reid, M. J., Menten, K. M., Genzel, R., Ott, T., Schödel, R., & Eckart, A. 2003, *ApJ*, in press
- Reid, M. J., Menten, K. M., Genzel, R., Ott, T., Schödel, R., & Brunthaler, A. to be published in *Astron. Nachr.*, Vol. 324, No. S1 (2003), Special Supplement "The central 300 parsecs of the Milky Way", Eds. A. Cotera, H. Falcke, T. R. Geballe, S. Markoff
- Rogers, Alan E. E., Doeleman, S., Wright, M.C.H., Bower, G.C., Backer, D.C., Padin, S., Philips, J.A., Emerson, D.T., Greenhill, L., Moran, J.M., Kellermann, K.I. 1994, *ApJ*, 434, L59
- Rousset G. 1998, in *Proc. SPIE Adapt. Opt. Tech.* (eds. D. Bonaccini & R.K. Tyson), 3353, 508
- Rubilar, G.F., & Eckart, A. 2001, *A&A*, 374, 95
- Salim, S., & Gould, A. 1999, *ApJ*, 523, 633

Schödel, R., Ott, T., Genzel, R., Hofmann, R., Lehnert, M., Eckart, A., Mouawad, N., Alexander, T., Reid, M. J., Lenzen, R., Hartung, M., Lacombe, F., Rouan, D., Gendron, E., Rousset, G., Lagrange, A.-M., Brandner, W., Ageorges, N., Lidman, C., Moorwood, A. F. M., Spyromilio, J., Hubin, N., & Menten, K. M. 2002, *Nature*, 419, 694

Torres, D.F., Capozziello, S., Lambiase, G. 2000, *Phys. Rev. D*, 63, id.104012

Tsiklauri, D., & Viollier, R.D. 1998, *ApJ*, 500, 591

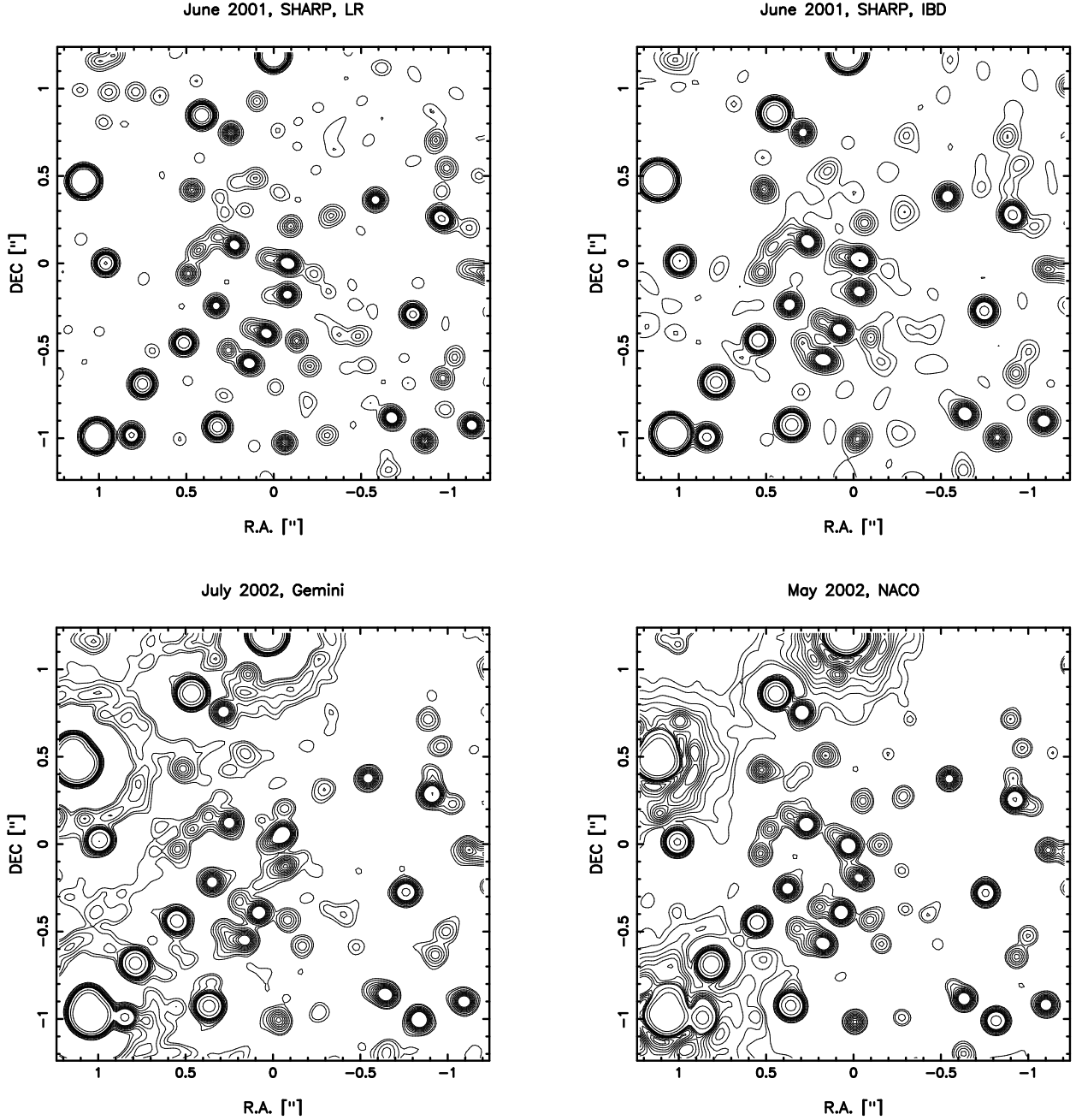


Fig. 1.— A comparison of high-resolution maps of the central $\sim 1.2'' \times 1.2''$ of the GC stellar cluster. The restoration beam FWHM was approximately 100 mas in all the images. Upper left: SHARP/NTT 2001, deconvolved with LR; upper right: SHARP/NTT 2001, deconvolved with IBD; lower left: Gemini 2000 (LR); lower right: NACO 2002 (LR). The bright sources at the left and upper edges of the field were saturated in the latter two data sets and show prominent deconvolution artifacts in form of rings. Contours at 10, 20, ... 90, 100, 200, 400% of the peak flux of S2, the bright source near the very center of the images.

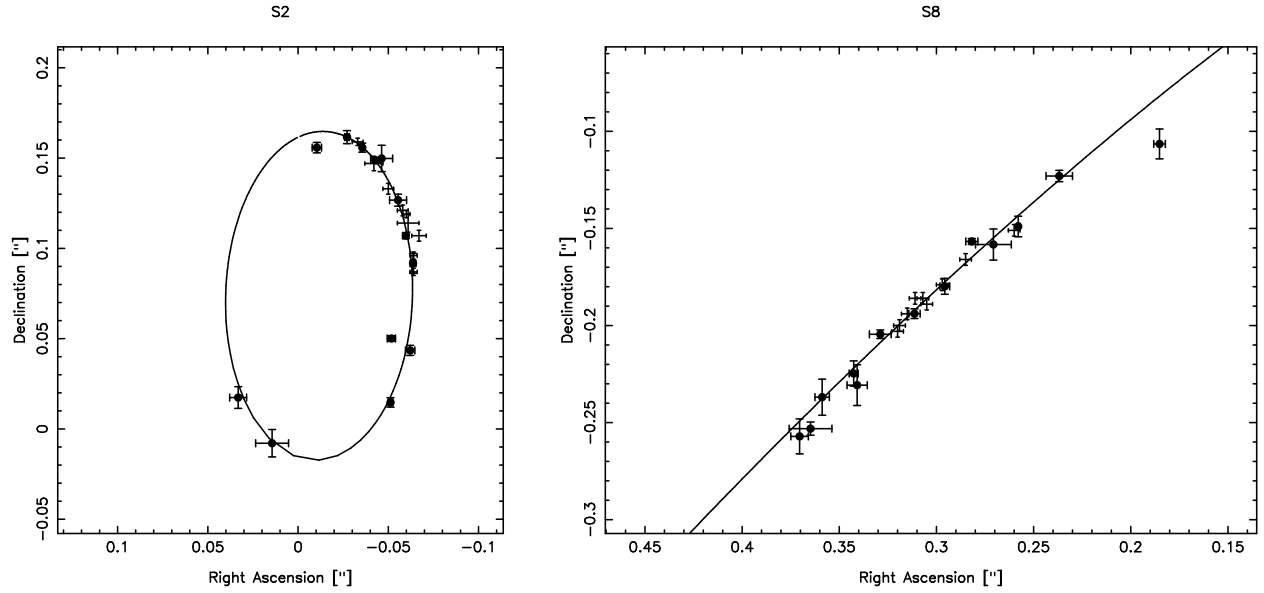


Fig. 2.— A comparison between positions of the stars S2 and S8 as measured by our group and by the Ghez et al. (2000) group. SHARP/NTT positions are marked by filled black circles with error bars, Keck positions just by their error bars. An offset of 40 mas W and 9 mas N (derived from the difference in position of S2 for the 1995 epoch) was applied to the Keck data in order to take into account the astrometric offset between the data sets. Straight lines mark the orbits fitted to the position of S2 and S8 (see section 5).

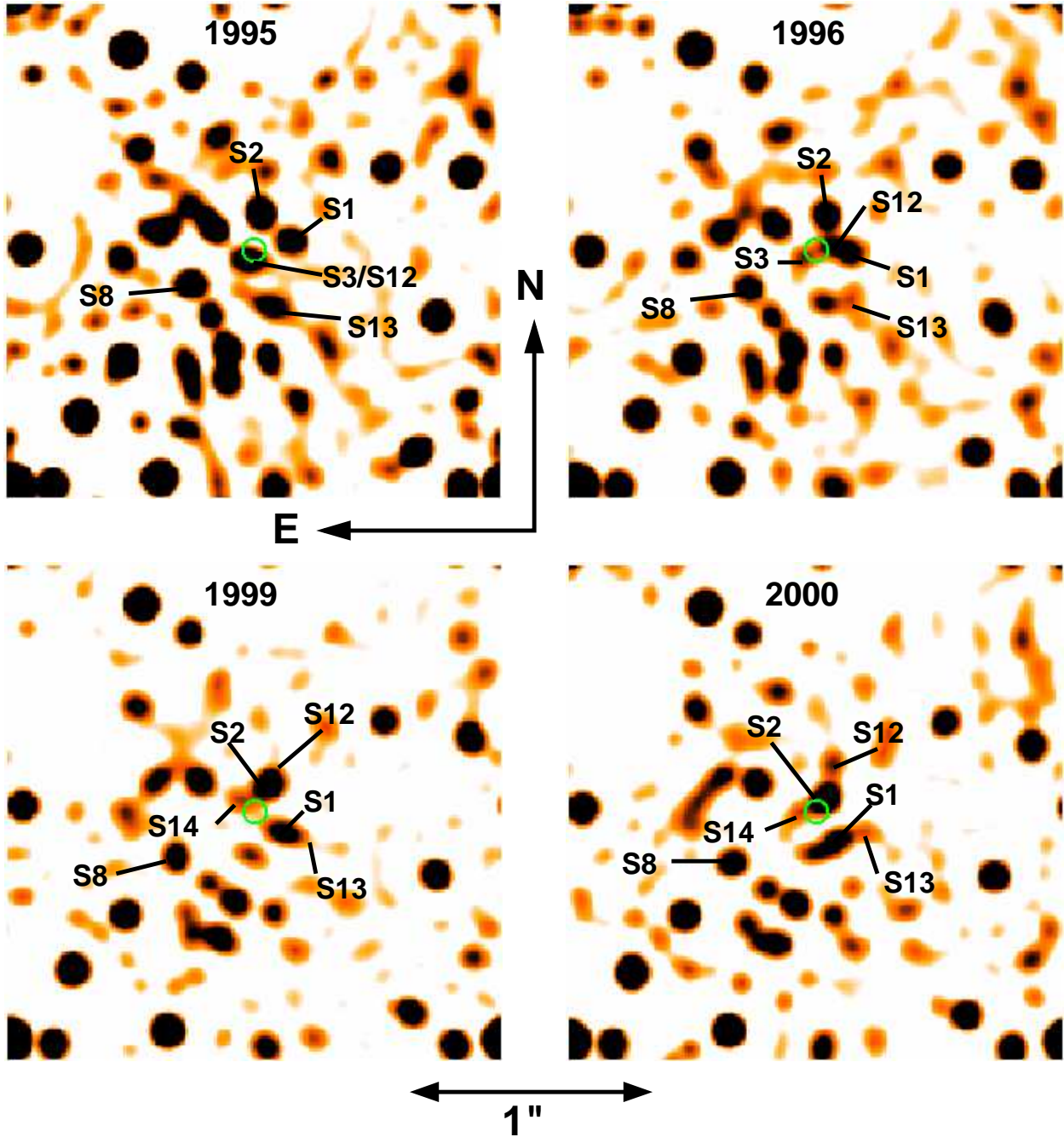


Fig. 3.— Identification of the sources S1, S2, S3, S8, S12, S13, and S14 for the epochs 1995.5, 1996.4, 1999.5, and 2000.5. The circle of ~ 50 mas radius marks the position of Sgr A*.

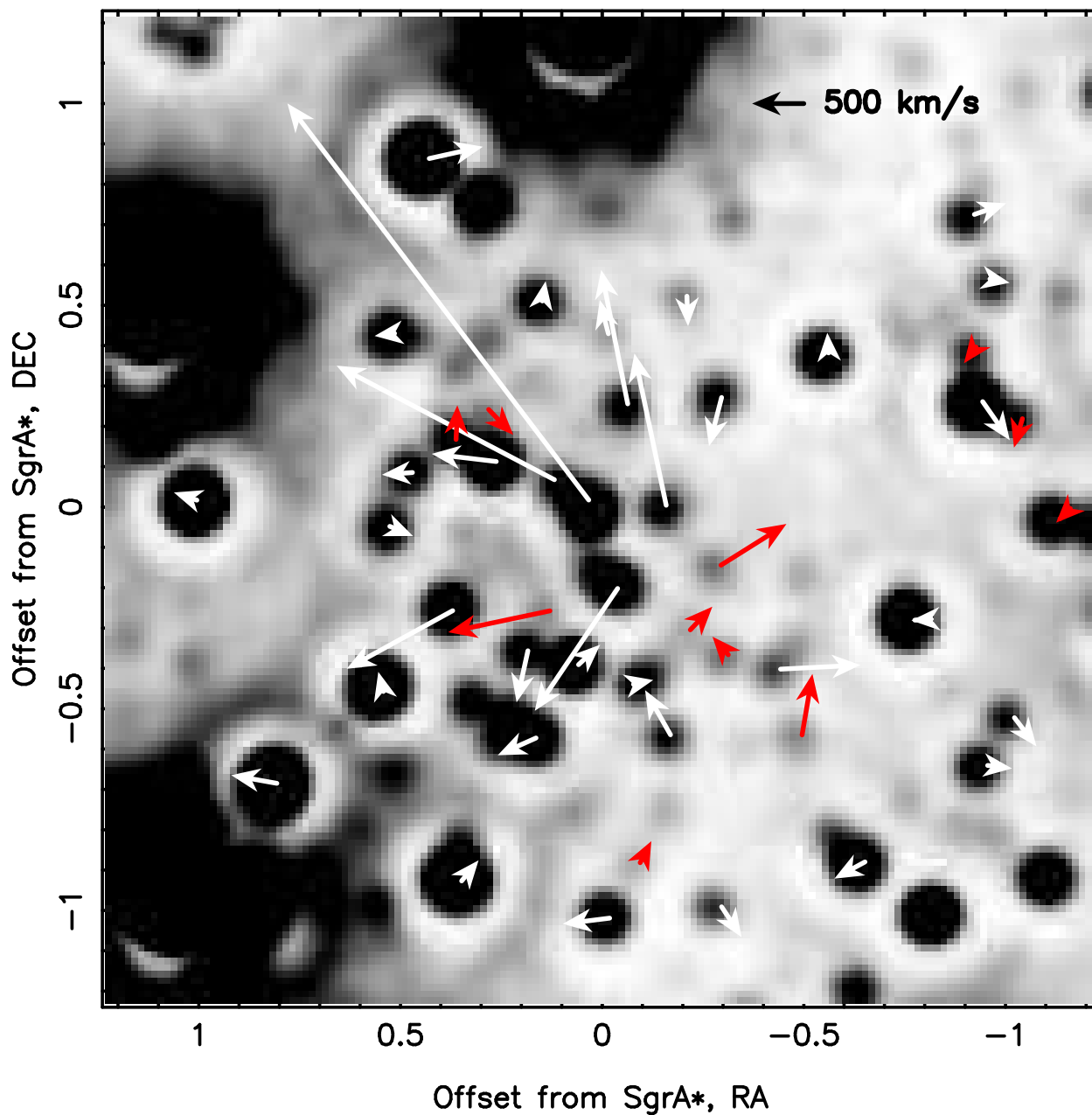


Fig. 4.— Stellar velocities within $1.2''$ of Sgr A*, superposed on a NACO 2002.4 image. Proper motions of the accelerated sources S1, S2, S8, S12, S13 and S14 are approximate estimates for this epoch. White arrows: Stars with proper motions based on the entire data set. Grey arrows: Stars with proper motions determined from the Gemini 2000 and the NACO August 2002 images only.

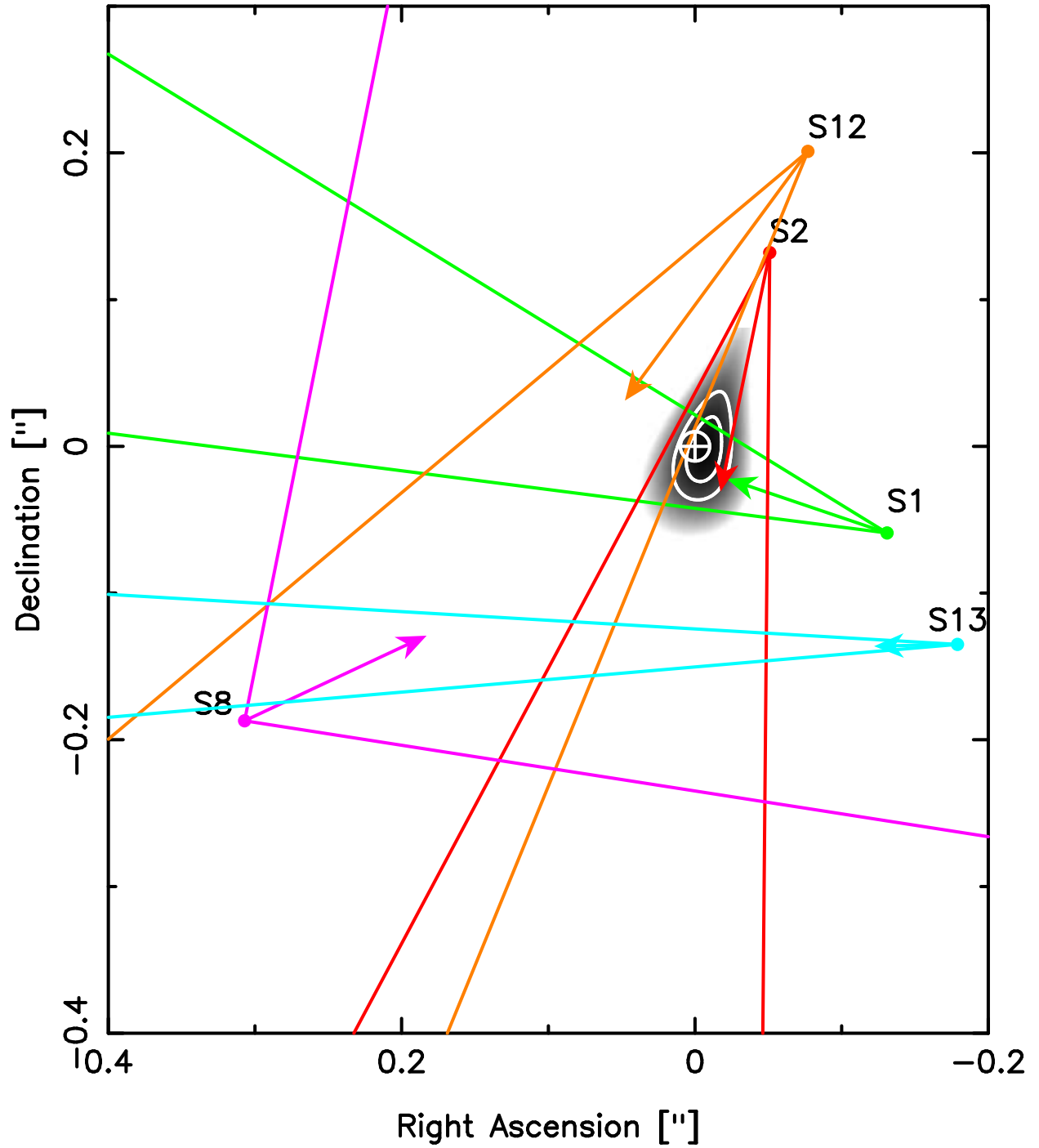


Fig. 5.— Projected average acceleration vectors with their 2σ error cones for the stars S1, S2, S8, S12, and S13. A χ^2 map of the position of the center of acceleration is overlaid in grey shades. White contours designate the 1 and 2σ confidence levels.

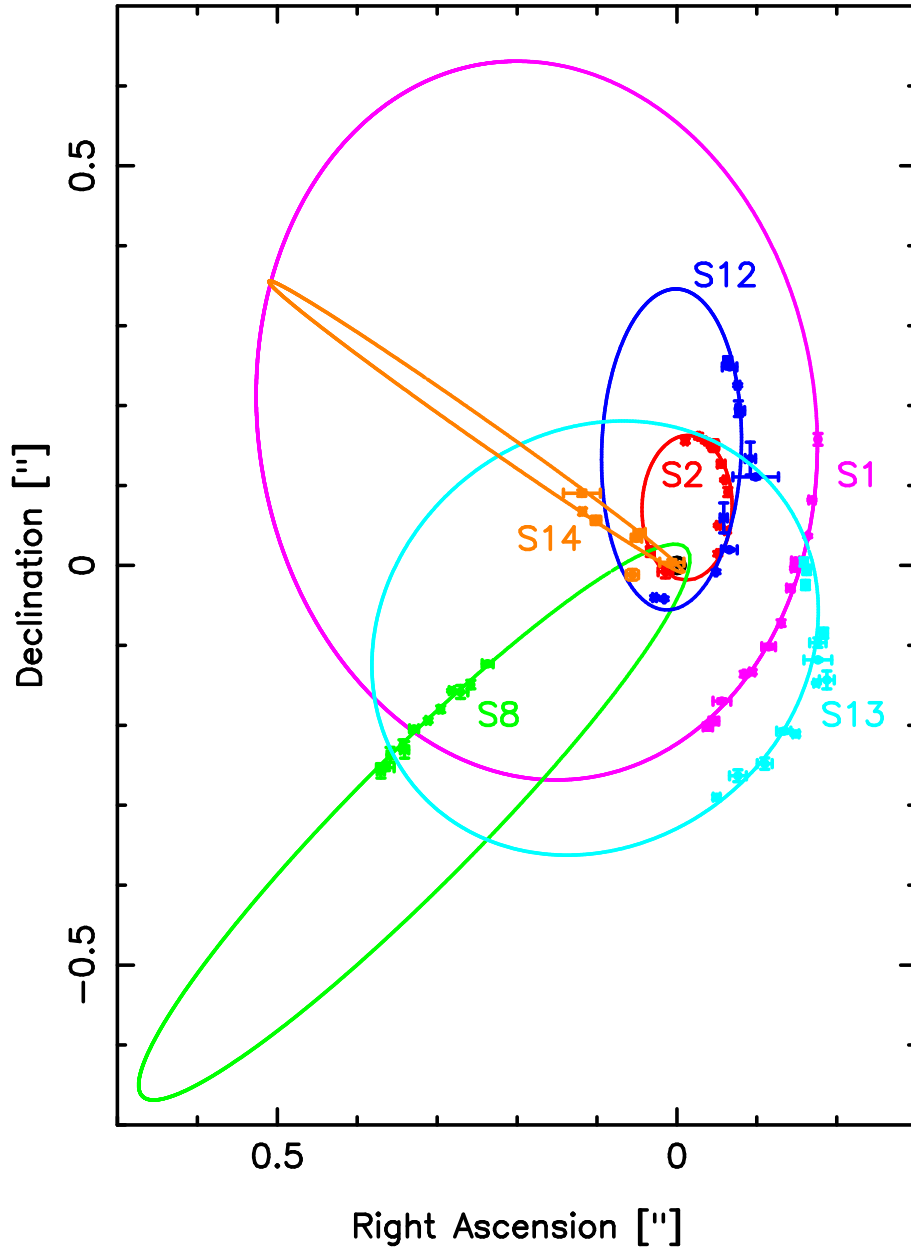


Fig. 6.— The measured time dependent positions with their errors and the determined projected orbits of the stars S1, S2, S8, S12, S13, and S14. The corresponding orbital parameters are listed in Table 5.

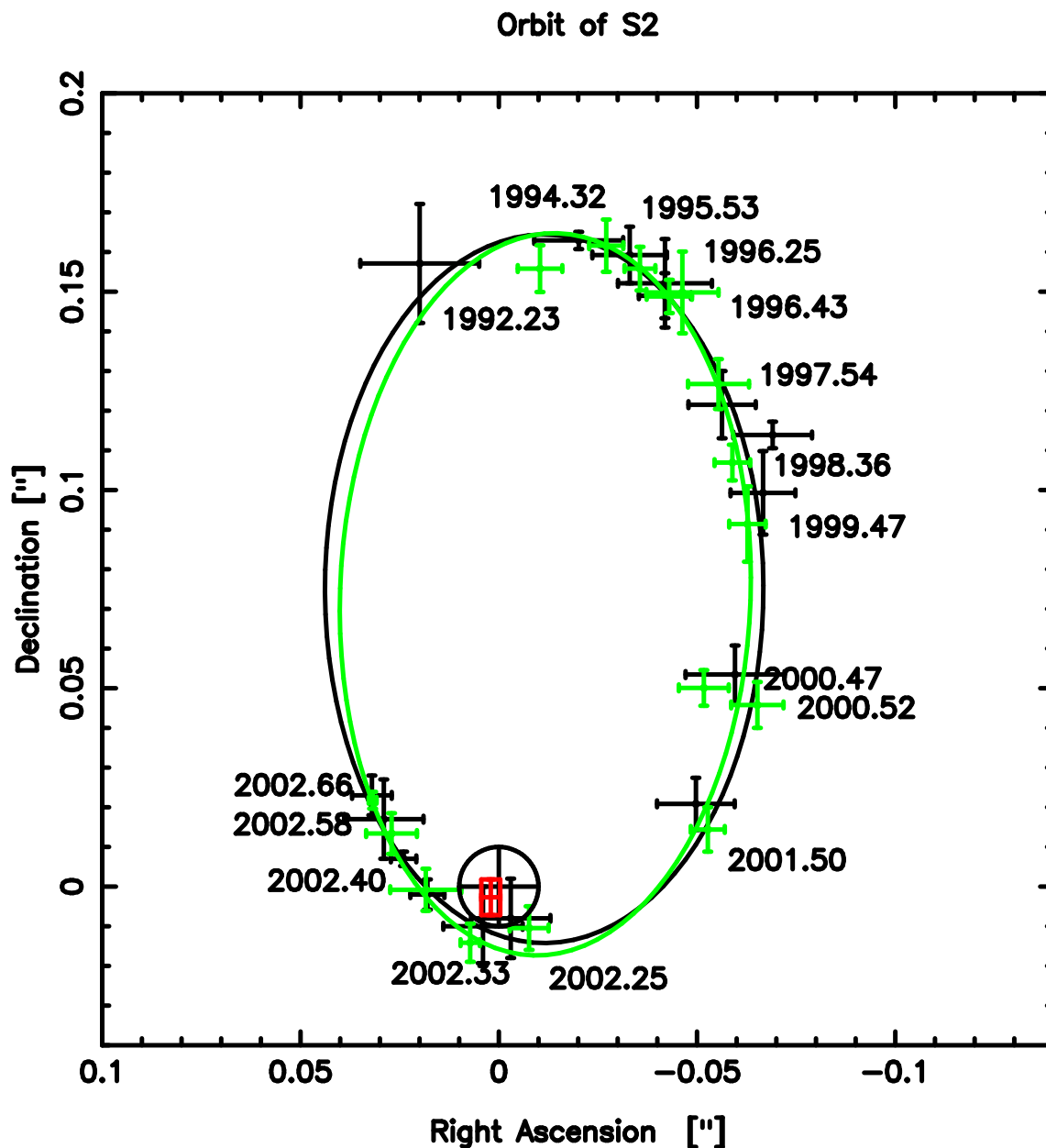


Fig. 7.— Comparison of the measured positions and orbital fits for S2 between this work (light grey) and Schödel et al. (2002) (black). The epoch labels refer to the positions from the present paper. The radio position of Sgr A* is marked by a black cross and a 10 mas error circle. The rectangular box within this circle marks the position of the focus of the orbit and its errors as determined in the present work.

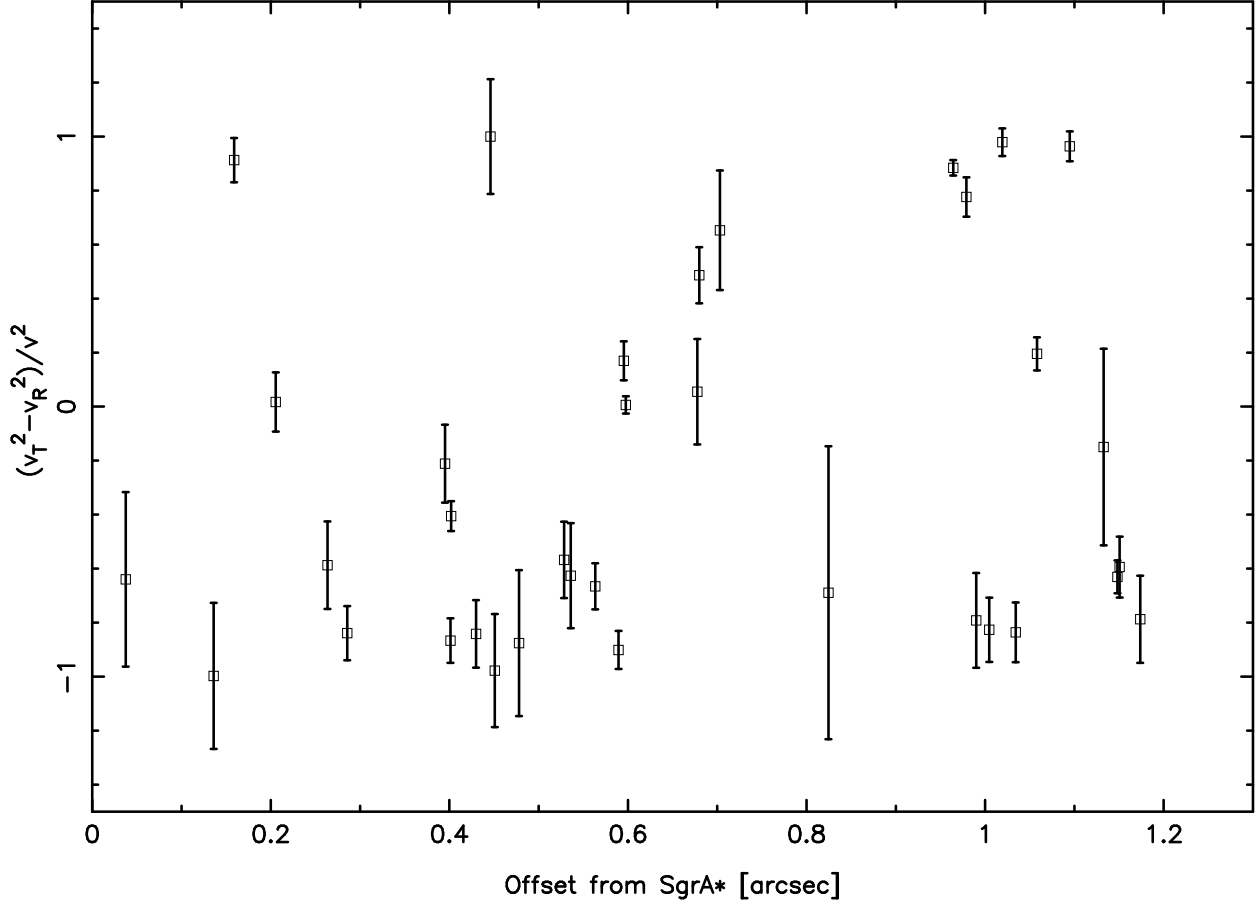


Fig. 8.— The anisotropy parameter $\gamma_{TR} = (v_T^2 - v_R^2)/v^2$ plotted against the projected distance from Sgr A* (epoch 2002.7) for the stars in Table 1 with the proper motions determined on the base of the entire data set. v is the proper motion velocity and v_T and v_R are its projected radial and tangential components. The majority of the stars appear to be on radial orbits.

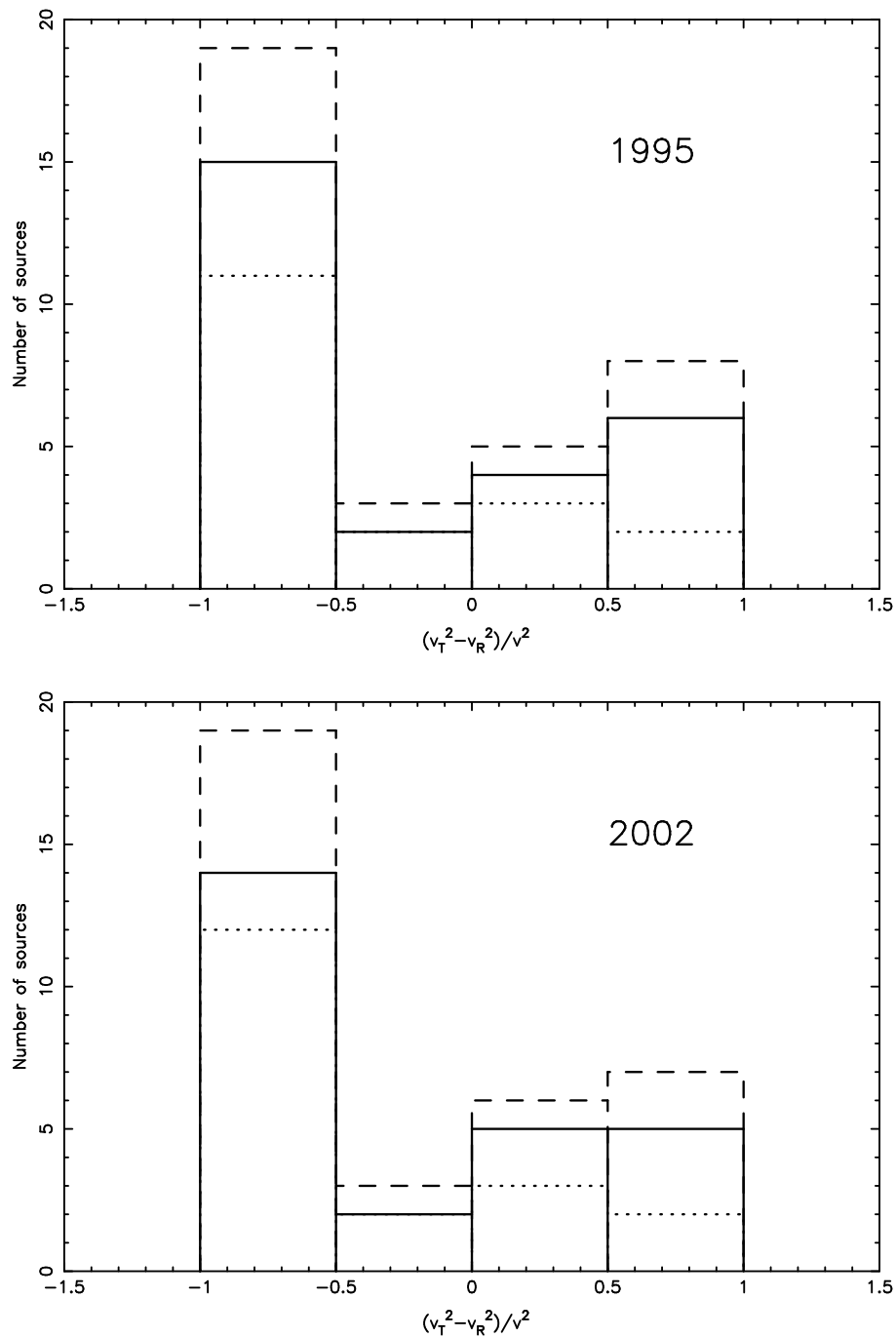


Fig. 9.— Histogram of the anisotropy parameter $\gamma_{TR} = (v_T^2 - v_R^2)/v^2$. v is the proper motion velocity and v_T and v_R are its projected radial and tangential components. Upper panel: 1995.5; lower panel: 2002.7. Dotted lines: Stars at projected distances $< 0.6''$ from Sgr A*; solid lines: stars at projected distances $< 1''$; dashed lines: stars at projected distances $< 1.2''$.

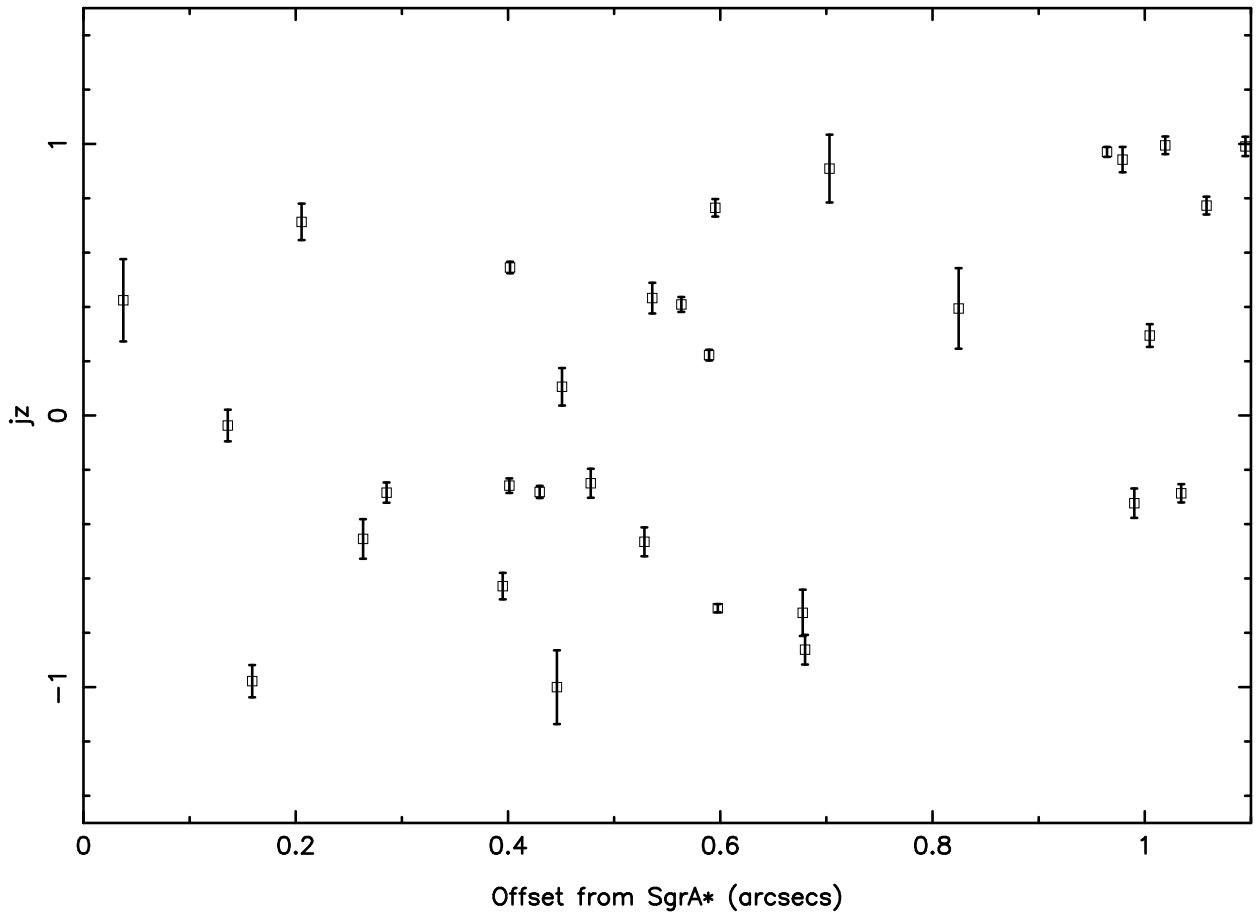


Fig. 10.— The normalized angular momentum $J_z/J_{z,\max} = (xv_y - yv_x)/pv_p$ in the 2002.7 epoch for the stars with proper motions based on the entire ten year data set.

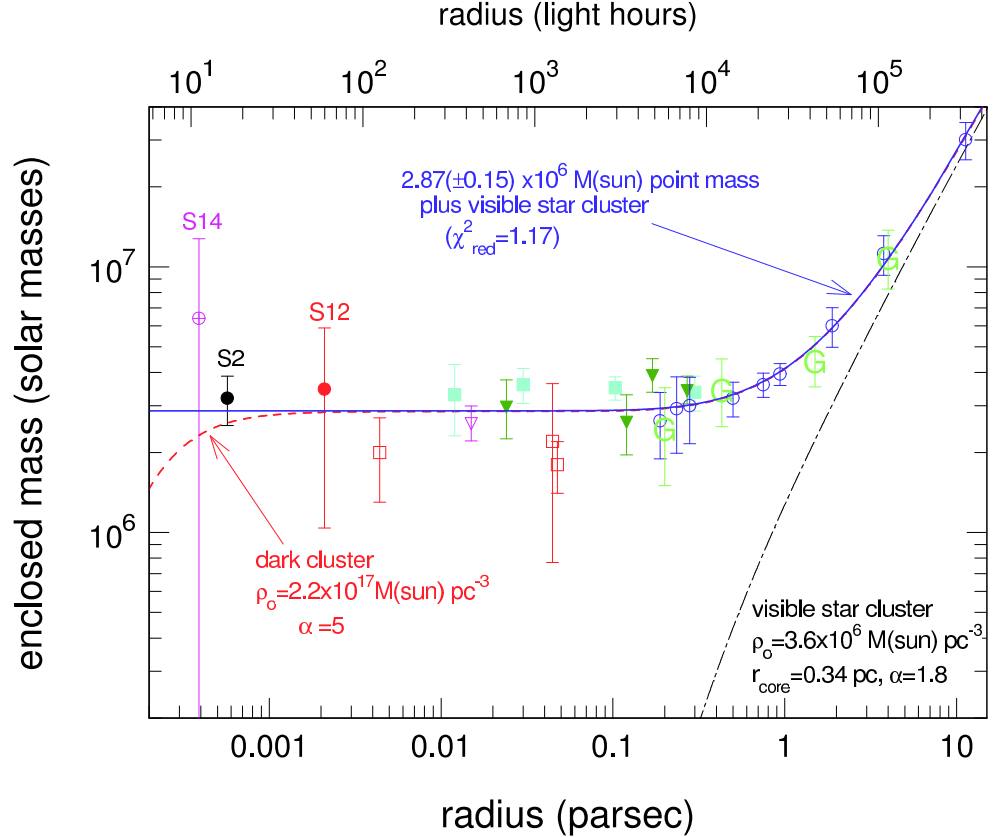


Fig. 11.— Mass distribution in the Galactic Center assuming an 8 kpc distance (Reid 1993). The circles at the shortest projected distances denote the masses derived from the orbits of S2, S12, and S14. Filled down pointing triangles denote Leonard-Merritt projected mass estimators from the present work (at 0.025 pc) and from a new NTT proper motion data set by Ott et al. (2003), separating late and early type stars, and correcting for the volume bias determined from Monte Carlo modeling of theoretical clusters and assuming a central density profile with a power-law slope of $\alpha = 1.37$ (Genzel et al. 2003). An open down-pointing triangle denotes the Bahcall-Tremaine mass estimate obtained from Keck proper motions (Ghez et al. 1998; we multiplied their error bar by a factor of 2 in order to take possible systematic errors into account). Filled rectangles are mass estimates from a parameterized Jeans-equation model, including effects of anisotropy and differentiating between late and early type stars (Genzel et al. 2000). Open circles are mass estimates from a parameterized Jeans-equation model of the radial velocities of late type stars, assuming isotropy (Genzel et al. 1996). Open rectangles denote mass estimates from a non-parametric, maximum likelihood model, assuming isotropy and combining late and early type stars (Chakrabarty & Saha 2001). The different statistical estimates (in part using the same or similar data) agree within their uncertainties but the variations show the sensitivity to the input assumptions. In contrast, the orbital technique for S2, S12, and S14 is much simpler and less affected by the assumptions. Letter “G” points denote mass estimates obtained from Doppler motions of gas (Genzel & Townes 1987). The straight continuous curve is the overall best fit model to all data. It is the sum of a $2.87 \pm 0.15 \times 10^6 M_{\odot}$ point mass, plus a stellar cluster of central density $3.6 \times 10^6 M_{\odot} \text{pc}^{-3}$, core radius 0.34 pc and power-law index $\alpha = 1.8$. The grey long dash-short dash curve shows the same stellar cluster separately, but for an infinitely small core. The dashed curve is the sum of the visible cluster, plus a Plummer model of a hypothetical very compact (core radius ~ 0.00019 pc) dark cluster of central density $2.2 \times 10^{17} M_{\odot} \text{pc}^{-3}$.

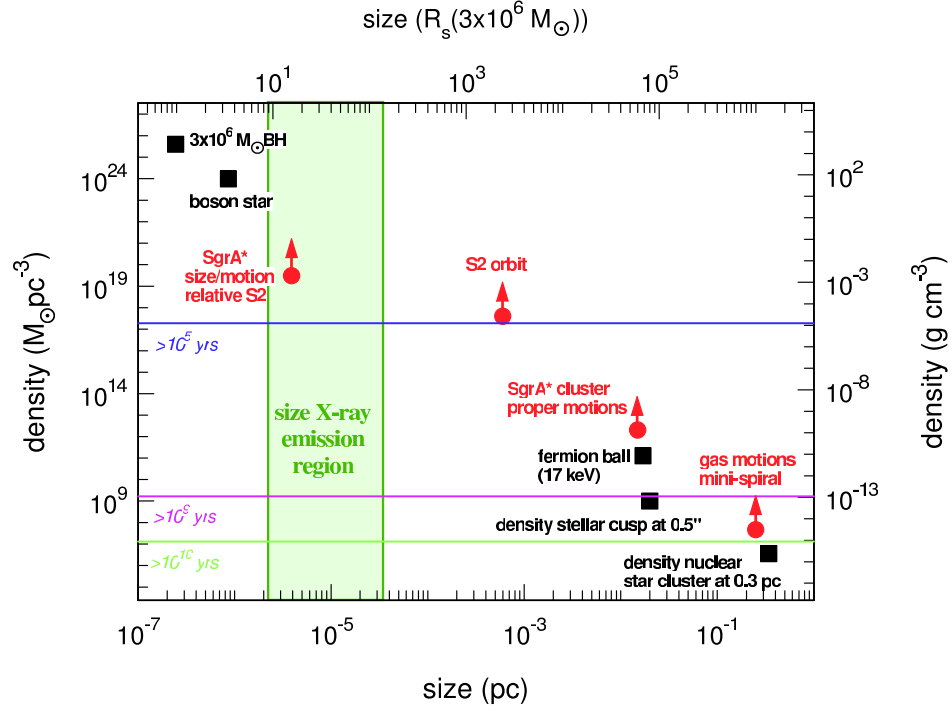


Fig. 12.— Constraints on the nature of the observed dark mass in the Galactic Center. The horizontal axis is the size (bottom in parsec, top in Schwarzschild radii), and the vertical axis the density (left: $M_{\odot}\text{pc}^{-3}$, right: g cm^{-3}). Filled circles denote the various limits on the size/density of the dark mass discussed in this paper. In addition the grey shaded area marks the constraints on the size of the variable X-ray emission from Baganoff et al. (2001). Large filled squares mark the location of different physical objects, including the visible star cluster and its central cusp, the heavy neutrino, fermion ball of Tsiklauri & Viollier (1998), the boson star of Torres et al. (2000) and, in the top left, the position of a $\sim 3 \times 10^6 M_{\odot}$ black hole. In addition three thin horizontal lines mark the lifetimes of hypothetical dark clusters of astrophysical objects, e.g. neutron stars, white dwarfs, or stellar black holes (Maoz 1998). The tightest constraints on the mass density come from the proper motion of Sgr A* compared to the velocities in the surrounding star cluster if one assumes additionally that the size of the dark mass is given by the millimeter radio measurements of Sgr A*. The now available measurements exclude all configurations but those of a black hole and a boson star.

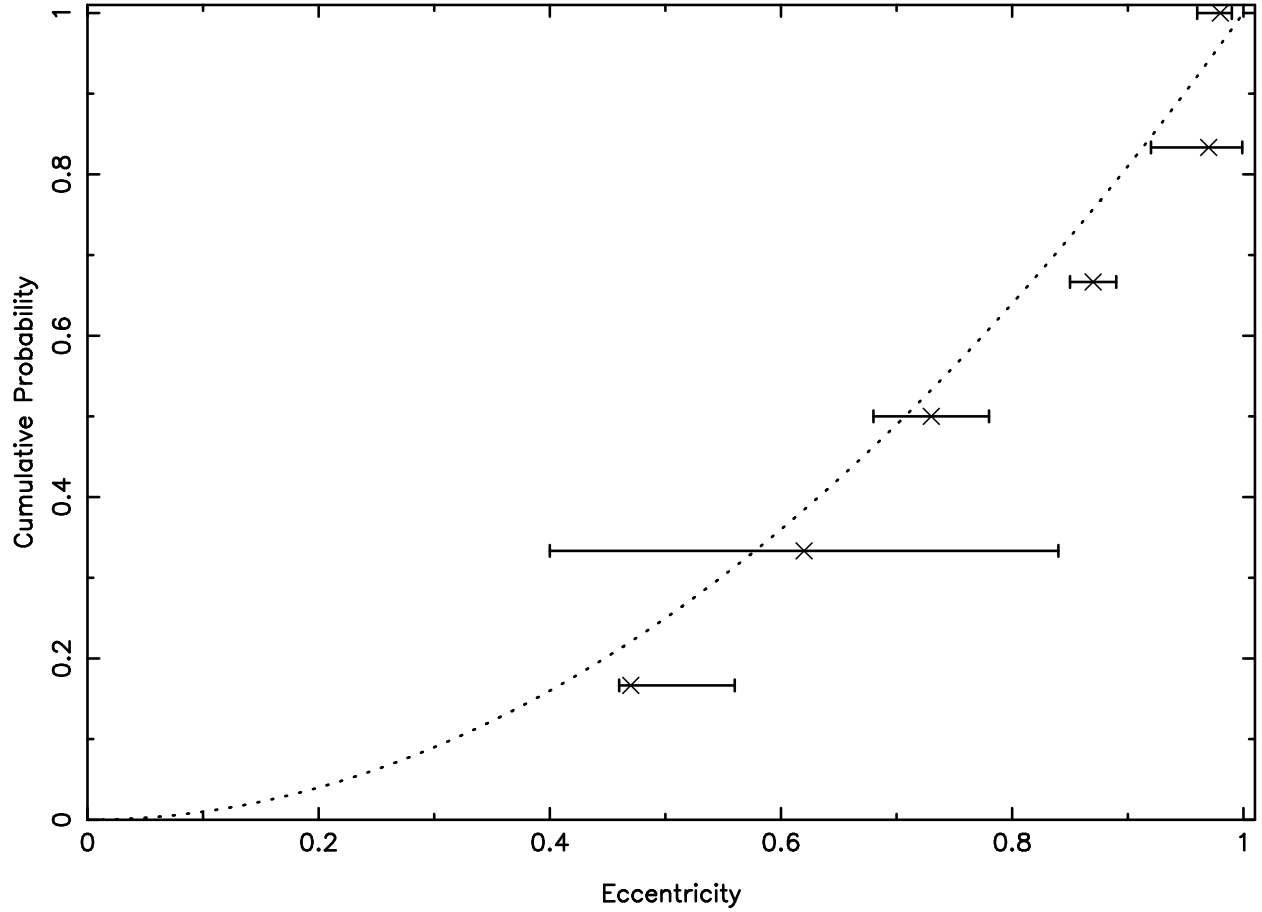


Fig. 13.— Dotted line: Cumulative probability distribution function of the eccentricities of test particles orbiting a point mass in a spherical, isotropic system. The crosses and their error bars mark the eccentricities measured for the 6 stars S1, S2, S8, S12, S13, and S14.

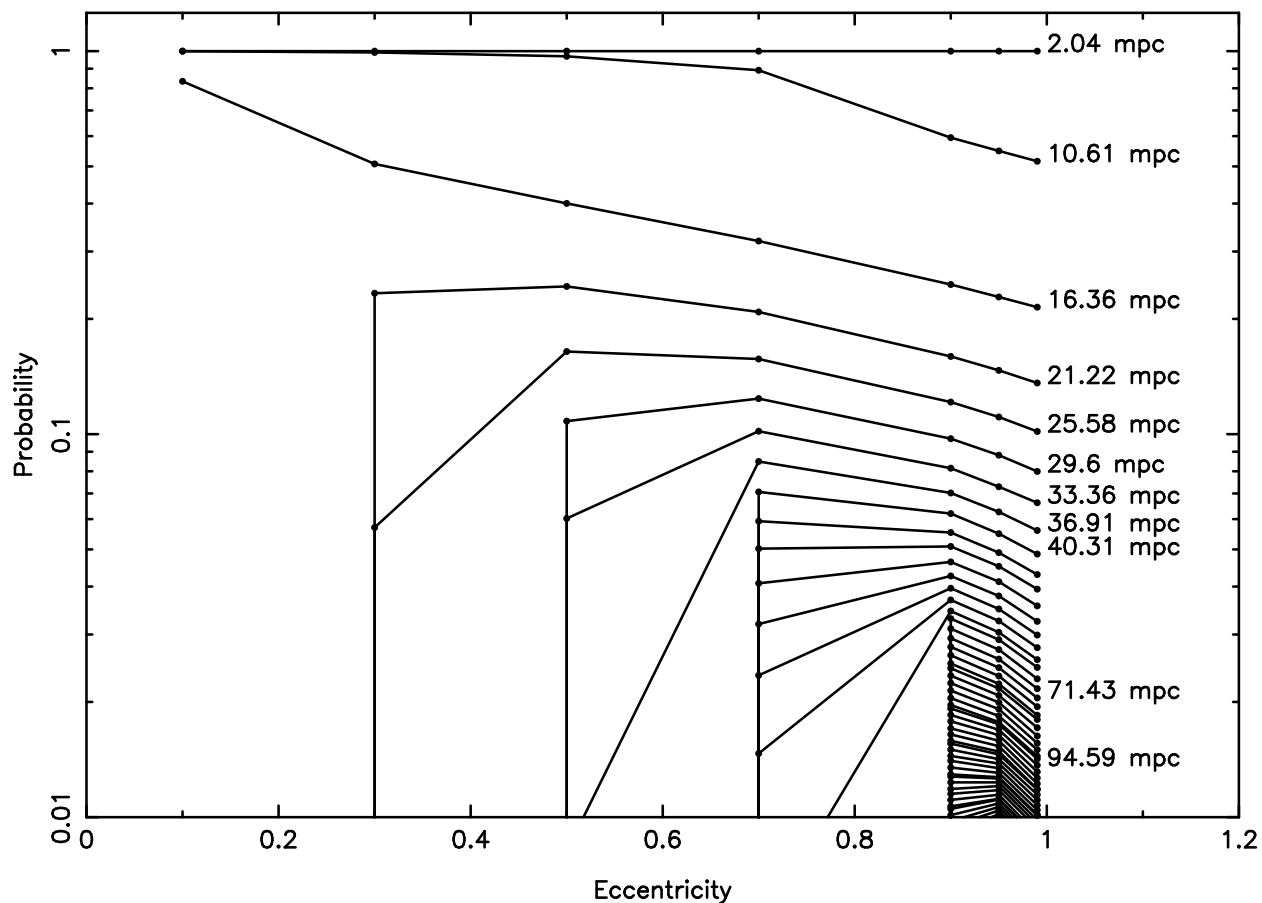


Fig. 14.— Probability of detecting a keplerian orbit with a given eccentricity e and semi-major axis a . The distribution of semimajor axes corresponds to the case of an isotropic stellar power-law cusp surrounding Sgr A*. A stellar density law of $n_* \propto r^{-3/2}$ has been assumed (Genzel et al. 2003). Values of the semi-major axes are given in the labels to the right of the curves. See text for explanations concerning the model leading to the respective probabilities. Curves for semimajor axes > 100 mpc were not plotted in order to avoid overcrowding the plot.

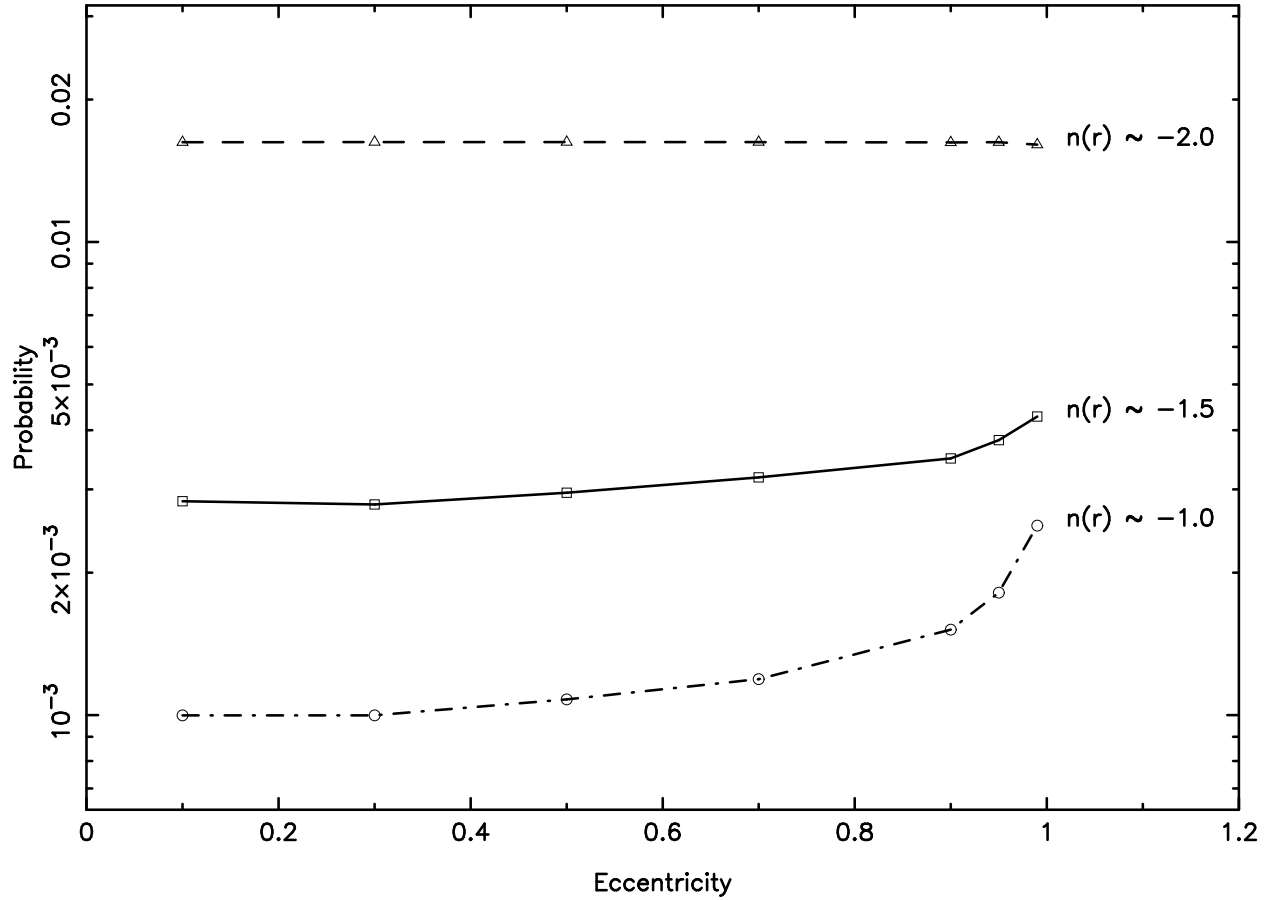


Fig. 15.— Overall detection bias of orbits with a given eccentricity assuming a power-law stellar cusp at the center of the Milky Way. The exponents of the cusps are plotted beside the corresponding curves. The probabilities were obtained after averaging over the detection probabilities for given distributions of semimajor axes such as shown in Figure 14. The overall low probabilities result from the fact that most stars have large semimajor axes.

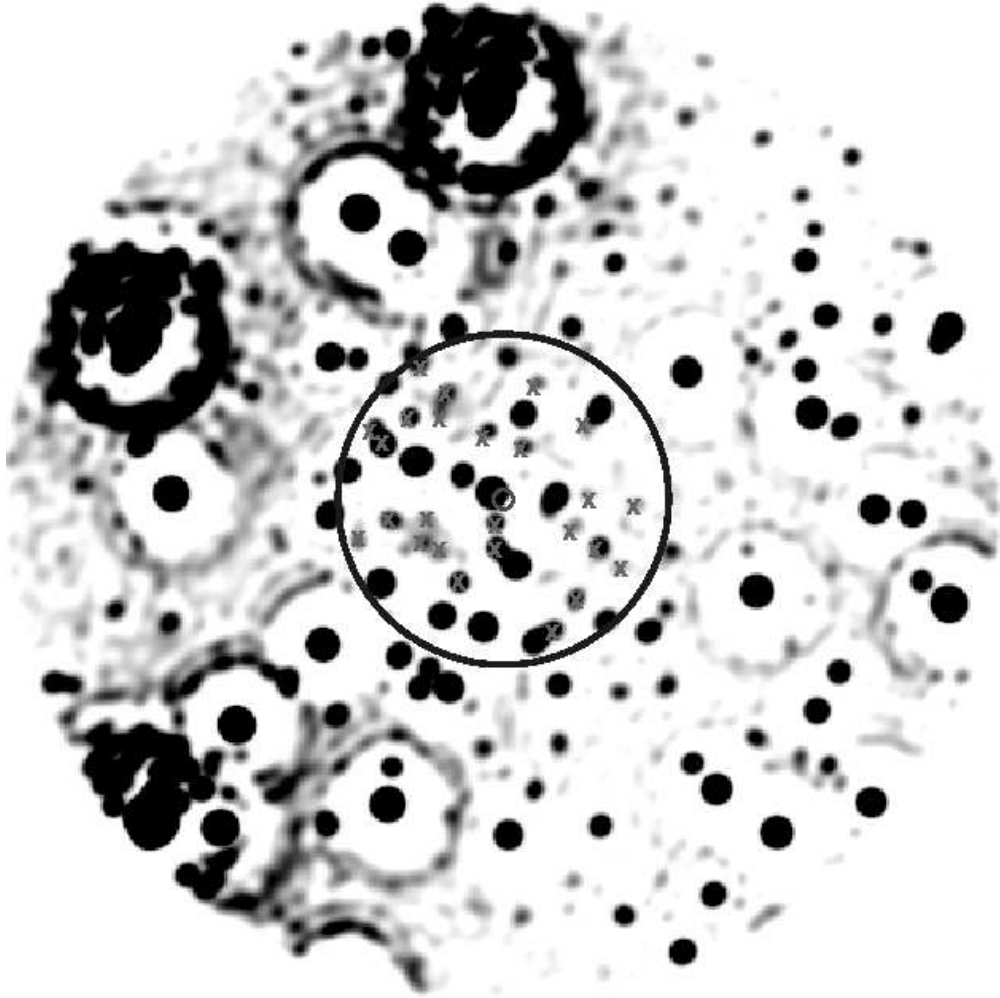


Fig. 16.— H-band map of the region $\leq 1.5''$ around Sgr A*, which is marked by a 30 mas radius circle. A 1500 s exposure shift-and-add image made with CONICA/NAOS in August 2002 was deconvolved with the Lucy-Richardson algorithm and smoothed to a FWHM of ~ 40 mas. Rings around brighter sources are artifacts of the deconvolution algorithm. The brightest sources are saturated. The large circle marks the region within $0.5''$ of Sgr A*. Some stars in that area with unknown or poorly known proper motions are marked with crosses.

Table 1. List of stars near Sgr A*.

ID	Name	R (arcsec)	M_K (mag)	dM_K (mag)	$\Delta R.A.$ (arcsec)	$d\Delta R.A.$ (arcsec)	ΔDEC (arcsec)	$d\Delta DEC$ (arcsec)	$V_{R.A.}$ (km s $^{-1}$)	$dV_{R.A.}$ (km s $^{-1}$)	V_{DEC} (km s $^{-1}$)	dV_{DEC} (km s $^{-1}$)
1	S2*, S0-2	0.037	13.9	0.1	0.033	0.005	0.017	0.006	2913	166	3834	42
2	S14*, S0-16	0.136	15.7	0.2	0.118	0.004	0.068	0.004	2106	190	1103	86
3	S13*, S0-20	0.159	15.8	0.3	-0.159	0.004	0.004	0.005	359	91	1483	48
4	S1*, S0-1	0.206	14.7	0.1	-0.039	0.006	-0.202	0.004	801	19	-1183	39
5	S12*, S0-19	0.263	15.5	0.2	-0.064	0.005	0.256	0.005	255	76	1098	52
6	S4, S0-3	0.286	14.4	0.1	0.262	0.004	0.113	0.008	623	17	74	14
7†	...	0.288	16.5	0.3	0.129	0.006	-0.257	0.007	984	187	-207	207
8†	...	0.328	16.9	0.3	-0.295	0.004	-0.144	0.002	-633	82	397	51
9†	...	0.371	16.4	0.3	0.281	0.007	0.242	0.003	-237	135	-246	93
10†	...	0.375	17.3	0.4	-0.219	0.003	-0.305	0.002	-213	74	225	98
11	S10, S0-6	0.395	14.2	0.1	0.059	0.009	-0.391	0.009	-210	9	193	15
12†	...	0.399	15.2	0.1	0.362	0.010	0.168	0.007	-12	180	330	185
13	S9, S0-5	0.401	15.1	0.1	0.184	0.004	-0.356	0.005	109	12	-499	11
14	, S0-8	0.402	15.8	0.3	-0.296	0.002	0.272	0.005	121	11	-471	6
15	...	0.43	17.0	0.4	-0.016	0.002	0.43	0.005	83	6	326	12
16	...	0.446	15.4	0.2	-0.1	0.007	-0.435	0.006	-105	10	23	12
17	S8*, S0-4	0.451	14.5	0.1	0.37	0.004	-0.257	0.009	536	40	-569	36
18	S6, S0-7	0.478	15.4	0.2	0.47	0.008	0.085	0.007	295	23	-21	14
19†	...	0.482	16.6	0.3	-0.313	0.01	-0.366	0.003	152	190	175	210
20	S7, S0-11	0.528	15.3	0.2	0.526	0.005	-0.048	0.006	-225	10	-93	12
21	...	0.536	15.6	0.2	0.148	0.003	0.515	0.003	-29	9	174	10
22	...	0.563	16.7	0.3	-0.21	0.004	0.523	0.004	-11	7	-290	7
23	...	0.589	15.7	0.2	-0.169	0.007	-0.565	0.007	244	7	431	9
24	S11, S0-9	0.595	14.4	0.1	0.164	0.009	-0.572	0.005	371	9	-167	12
25	...	0.598	16.2	0.2	-0.442	0.003	-0.402	0.004	-774	9	40	8
26	...	0.678	15.1	0.1	0.525	0.006	0.429	0.005	153	11	-20	10
27	W6, S0-12	0.68	14.4	0.1	-0.562	0.003	0.383	0.004	13	9	190	8
28	, S0-13	0.703	13.4	0.1	0.546	0.006	-0.443	0.009	34	13	132	12
29†	...	0.752	17.0	0.4	-0.496	0.004	-0.565	0.003	-99	64	590	110
30	W9, S0-14	0.825	13.8	0.1	-0.775	0.002	-0.28	0.004	34	6	-2	4
31†	...	0.887	17.0	0.3	-0.094	0.005	-0.882	0.005	-108	124	209	167
32	, S1-3	0.964	12.3	0.1	0.429	0.006	0.864	0.003	-518	6	115	9
33	W5, S0-15	0.979	13.7	0.1	-0.943	0.004	0.261	0.008	-262	11	-374	16
34	, S1-5	0.99	12.6	0.1	0.348	0.008	-0.927	0.005	-164	13	199	13

Table 1—Continued

ID	Name	R (arcsec)	M_K (mag)	dM_K (mag)	Δ R.A. (arcsec)	$d\Delta$ R.A. (arcsec)	Δ DEC (arcsec)	$d\Delta$ DEC (arcsec)	$V_{R.A.}$ (km s ⁻¹)	$dV_{R.A.}$ (km s ⁻¹)	V_{DEC} (km s ⁻¹)	dV_{DEC} (km s ⁻¹)
35†	...	1.003	15.6	0.1	-0.924	0.006	0.392	0.004	103	162	-140	144
36	, S1-1	1.005	13.2	0.1	1.005	0.005	0.017	0.004	223	8	73	9
37	, S1-2	1.019	14.9	0.1	-0.019	0.004	-1.019	0.004	453	10	-55	13
38	...	1.034	16.1	0.1	-0.296	0.003	-0.991	0.004	-193	11	-294	11
39	, S1-4	1.058	12.6	0.1	0.806	0.004	-0.685	0.005	441	8	80	15
40†	...	1.065	15.8	0.3	-1.042	0.004	0.219	0.003	82	135	-280	111
41	, S1-8	1.095	14.2	0.1	-0.652	0.003	-0.88	0.007	296	8	-162	9
42	...	1.133	15.7	0.1	-0.984	0.005	0.561	0.007	-102	13	-20	14
43†	...	1.135	14.8	0.1	-1.135	0.004	-0.029	0.005	37	83	-37	119
44	, S1-7	1.148	15.8	0.1	-1.023	0.003	-0.522	0.005	-212	5	-277	8
45	...	1.151	15.3	0.1	-0.956	0.003	-0.641	0.006	-236	6	-29	13
46	, S1-6	1.174	15.6	0.1	-0.923	0.007	0.725	0.008	-309	15	107	15

Note. — List of stars within 1.2'' of Sgr A*. Stars marked with an asterisk show accelerated movement. The velocities given for these stars are approximate velocities for the 2002.7 epoch, derived from a linear fit to a subset of the positional data. Positions and magnitudes are for the epoch 2002.66. An additional general ~ 0.1 magnitude systematic error should be taken into account because of uncertainties in the fluxes of the calibration sources. Proper motions of stars marked with a † are based solely on the Gemini/NACO data subset as described in the text. Names behind a comma in column 2 refer to names assigned by Ghez et al. (1998), except S0-16, S0-19, and S0-20, which refer to (Ghez et al. 2003a). In section 5 we estimate an additional systematic error of the order 0.003'' on the positions at all epochs. That corresponds to an additional error of ~ 20 km/s in the proper motion velocities.

Table 2. List of stars near Sgr A* with measured average accelerations from parabolic fits to sections of their orbits.

ID	Name	Epoch (yr)	Δ R.A. (arcsec)	Δ DEC (arcsec)	a (mas yr ⁻²)	da (mas yr ⁻²)	$a_{R.A.}$ (mas yr ⁻²)	$da_{R.A.}$ (mas yr ⁻²)	a_{DEC} (mas yr ⁻²)	da_{DEC} (mas yr ⁻²)
1	S2	1997.25	-0.051	0.132	5.55	0.66	1.12	0.53	-5.43	0.67
3	S13	1998.38	-0.179	-0.135	5.70	0.30	5.69	0.30	-0.12	0.21
4	S1	1998.16	-0.131	-0.059	3.84	0.27	3.64	0.25	1.23	0.35
5	S12	2000.75	-0.077	0.201	7.03	0.57	4.16	0.73	-5.66	0.47
17	S8	1998.16	0.307	-0.187	1.37	0.46	-1.24	0.47	0.58	0.46

Table 3. Projected accelerations, projected masses and inclination angles, determined from parabolic fits.

ID	Name	a (mas yr ⁻²)	da (mas yr ⁻²)	$M_{proj} = M_{BH} * \cos(i)^3$ $10^6 \times M_{\odot}$	i deg	di deg
1	S2	5.55	0.66	1.5	37	6
3	S13	5.70	0.30	4.48	n.a.	n.a.
4	S1	3.84	0.27	0.89	47	5
5	S12	7.03	0.57	4.34	n.a.	n.a.
17	S8	1.37	0.46	2.50	17	42

Table 4: Orbital parameters of S2 as determined for normal (column 1) and equal weighting (column 2) of the measured positions. In the third column we list the orbital parameters of S2 according to Ghez et al. (2003). Offsets are measured positive to the East and North.

Weighting	Normal	Equal	Ghez et al.
Offset R.A. (mas)	2.0 ± 2.4	1.4 ± 1.3	-2.7 ± 1.9
Offset Decl. (mas)	-2.7 ± 4.5	-2.3 ± 3.1	-5.4 ± 1.4
Central Mass ($10^6 M_{\odot}$)	3.31 ± 0.67	3.07 ± 0.72	4.07 ± 0.68
Period (yr)	15.73 ± 0.74	15.31 ± 0.71	15.78 ± 0.82
Pericenter Passage (yr)	2002.31 ± 0.02	2002.31 ± 0.04	2002.33 ± 0.02
Eccentricity	0.87 ± 0.02	0.87 ± 0.02	0.87 ± 0.01
Angle of line of nodes (deg)	44.2 ± 7.0	49.1 ± 8.2	40.1 ± 3.0
Inclination (deg)	$\pm 45.7 \pm 2.6$	$\pm 44.7 \pm 3.9$	-47.3 ± 2.5
Angle of node to pericenter (deg)	$244.7.1 \pm 4.7$	241.0 ± 6.3	251.4 ± 1.8
Semi-major axis (mpc)	4.54 ± 0.27	4.34 ± 0.31	4.87 ± 0.21
Separation of pericenter (mpc)	0.59 ± 0.10	0.56 ± 0.10	0.61 ± 0.05

Table 5: Parameters and their formal uncertainties for the orbits of S1, S2, S8, S12, S13 and S14. The position of the focus has been fitted simultaneously in the case of S2. For the other stars, additional astrometric errors of the parameters must be taken into account because of the uncertainty in the position of the gravitational focus. These errors are of the same order as the fitting errors.

	S2	S12	S14	S1	S8	S13
Central Mass ($10^6 M_\odot$)	3.3 ± 0.7	3.5 ± 1.8	6.4 ± 7.6	$2.6^{2.1}_{3.5}$	$1.9^{1.6}_{3.1}$	$2.3^{2.2}_{2.9}$
Period (yr)	15.73 ± 0.74	36.0 ± 8.3	69.0 ± 26.6	171^{602}_{86}	342^{473}_{148}	75^{75}_{148}
Pericenter Passage (yr)	2002.31 ± 0.02	1995.3 ± 0.3	1999.9 ± 0.2	$1999.6^{1999.1}_{2000.6}$	2330^{2481}_{2134}	$2005.4^{2005.4}_{2005.1}$
Eccentricity	0.87 ± 0.02	0.73 ± 0.13	0.97 ± 0.05	$0.62^{0.84}_{0.40}$	$0.98^{0.99}_{0.96}$	$0.47^{0.46}_{0.56}$
Angle of line of nodes (deg)	44.2 ± 7.0	99.9 ± 2.3	40.2 ± 3.0	104^{103}_{105}	109^{106}_{124}	173^{138}_{175}
Inclination (deg)	45.7 ± 2.6	52.6 ± 6.9	82.6 ± 0.5	45^{40}_{50}	30^{10}_{60}	10^{0}_{30}
Angle of node to pericenter (deg)	$244.7.1 \pm 4.7$	159.9 ± 16.3	143.0 ± 19.5	114^{111}_{122}	25^{25}_{33}	325^{0}_{320}
Semi-major axis (mpc)	4.54 ± 0.27	8.0 ± 0.7	15.1 ± 4.6	21^{45}_{14}	29^{34}_{20}	11^{11}_{13}
Separation of pericenter (mpc)	0.59 ± 0.10	2.2 ± 0.4	0.39 ± 0.78	8^7_9	$0.6^{0.3}_{0.8}$	6^6_6

Table 6: Table of enclosed mass estimates from proper motions of stars within $1.2''$ of Sgr A*. We compiled four lists of stellar proper motions: 2 short lists including 35 proper motions from the entire SHARP/Gemini/NACO data set and 2 long lists (LL) including additionally the (larger error) proper motions of 11 sources solely based on the Gemini July 2000/NACO September 2002 images. For the 6 stars with measured accelerated motion, we determined velocities at two different epochs each and included them in the short and long lists (SL1, SL2, LL1, LL2). N is the number of stars in the respective list, p is the projected distance from Sgr A* (please refer to Bahcall & Tremaine 1981 for the meaning of the expression $2/\pi/\langle 1/p \rangle$), M_{LM} is the Lonard-Merritt mass estimator, σ_R is the projected radial and σ_T the projected tangential velocity dispersion.

List	N	$2/\pi/\langle 1/p \rangle$ ($''$)	M_{LM} $1 \times 10^6 M_\odot$	σ_R $1 \times 10^6 M_\odot$	σ_T/σ_R
SL1	35	0.58	3.7 ± 0.9	840 ± 104	0.66 ± 0.12
SL2	35	0.67	3.7 ± 0.9	540 ± 67	0.78 ± 0.12
LL1	46	0.61	3.3 ± 0.7	745 ± 78	0.68 ± 0.10
LL2	46	0.68	3.1 ± 0.7	498 ± 52	0.98 ± 0.14

Table 7: Different mass estimates for the central point mass (in $10^6 M_\odot$). Column 1: Mass estimate from the orbit of S2 (this work). Column 2: Mass estimate from the orbit of S2 as determined by Ghez et al. (2003a). Column 3: Average mass estimate from three stellar orbits by Ghez et al. (2003a). Column 4: Average LM mass estimate from proper motions within $1.2''$ of SgrA* (this work). Column 5: Mass estimate from fit to all available measurements within ~ 1 pc of Sgr A* (see Figure 11, this work). Column 6: Like column 5, without the systematically low estimates (see section 7.1).

$M_{S2,1}$	$M_{S2,2}$	$M_{3orbits}$	$M_{LM} (< 1.2'')$	Fit ₁	Fit ₂
3.3 ± 0.7	4.1 ± 0.6	3.6 ± 0.4	3.4 ± 0.5	2.9 ± 0.2	3.1 ± 0.2